Acta Materialia 266 (2024) 119657

Contents lists available at ScienceDirect

Acta Materialia

journal homepage: www.elsevier.com/locate/actamat

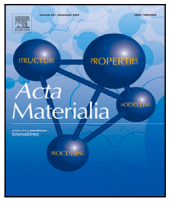

Full length article

Micro-strain and cyclic slip accumulation in a polycrystalline nickel-based superalloy

R.L. Black [a], D. Anjaria [a], J. Genée [b], V. Valle [c], J.C. Stinville [a,*]

[a] University of Illinois Urbana-Champaign, Urbana, USA
[b] Institut Clement Ader (ICA) - UMR CNRS 5312, Université de Toulouse, CNRS, INSA, UPS, Mines Albi, ISAE-SUPAERO, Albi, France
[c] Institut PPRIME, Université de Poitiers, CNRS, ENSMA, Chasseneuil, France

ARTICLE INFO

Keywords:
Polycrystalline nickel-based superalloy
Fatigue crack nucleation
Cyclic slip irreversibility
Strain localization
High-resolution digital image correlation

ABSTRACT

This work provides a comprehensive characterization and analysis of deformation and fatigue damage mechanisms in a nickel-based superalloy during ambient temperature fatigue and points to a fundamental deformation mechanism that results in the onset of crack nucleation. Strain and slip irreversibility are investigated at the nanometer scale using high-resolution digital image correlation and high-resolution electron backscatter diffraction, highlighting distinct deformation mechanisms contributing to crack nucleation. It is observed during early fatigue cycling at relatively low applied stress, the formation of intense slip events that induce grain boundary shearing. This results in intense micro-scale strain in the neighboring grains, producing localized plasticity and stresses. Such stresses facilitate fatigue extrusion–intrusion mechanisms during subsequent cycling, resulting in preferred crack nucleation. Finally, the configurations within the microstructure that promote such deformation and damage mechanisms sequence are highlighted.

This is a **colorblind-friendly version** (protanopia, deuteranopia, tritanopia). Figures were remade using the ImageJ "Replace Red with Magenta" plug-in under the Image > Color menu, see Ref. [1]., the use of the Parrot LUT, see Ref. [2], and through custom edits. The colorblind version of this article has been made possible thanks to funding from the NSF (award #2338346).

1. Introduction

Fatigue damage in polycrystalline metals originates from sub-grain-scale plasticity, as documented by various researchers [3–5]. In materials that undergo deformation by slip, fatigue damage is primarily influenced by cyclic slip irreversibility. This phenomenon arises due to the accumulation of plasticity caused by the motion of dislocations, which are not entirely recovered during the reverse part of a fatigue cycle [3,6–11]. Particular regions within the microstructure of a specimen are susceptible to developing intense cyclic slip irreversibility, leading to either persistent slip bands (PSBs) or sub-grain-scale fatigue shear bands; these features eventually result in crack nucleation [3–5].

Multiple physical and microstructural factors influence cyclic slip irreversibility and crack nucleation in metals and alloys. Notably, the crystal structure and microstructure of materials play a crucial role in determining the intensity of cyclic slip irreversibility, which in turn governs their fatigue strength [12]. For precipitation-strengthened nickel-based superalloys, low fatigue ratios (fatigue strength divided by yield or ultimate tensile strength) are observed [12]. This low fatigue ratio is associated with the tendency of alloys to form intense slip localization with a high degree of irreversibility due to the presence of small scale precipitates [3,9,12–14]. Intense slip localization is typically found near and parallel to coherent twin boundaries (CTB), leading to crack nucleation associated with CTBs [15,16]. Material elastic anisotropy causes local stress concentrations near CTBs [17], which significantly enhances dislocation glide near these boundaries [18]. Since a slip plane aligns with CTBs, dislocations can move freely along the boundary and traverse the entire grain diameter, favoring intense slip localization in the vicinity of CTBs [8,13,19]. Furthermore, the extent of slip localization intensifies with the length of the slip plane, a phenomenon initially documented by Peralta et al. [20] and Kim and Laird [21]. This phenomenon occasionally results in a high level of slip irreversibility during cyclic loading [9] and ultimately leads to crack nucleation. Furthermore, CTBs form triple junctions (or triple junction lines), which can promote stress concentration, further intensifying slip localization [22,23]. Concurrently, certain superalloys exhibit disruption in the precipitate state near CTBs, contributing to increased slip localization and crack nucleation [24,25].

While damage nucleation is typically linked to high levels of slip localization and slip irreversibility, evidence has shown that CTBs that

* Corresponding author.
E-mail address: jcstinv@illinois.edu (J.C. Stinville).

https://doi.org/10.1016/j.actamat.2024.119657
Received 9 September 2023; Received in revised form 5 January 2024; Accepted 5 January 2024
Available online 9 January 2024

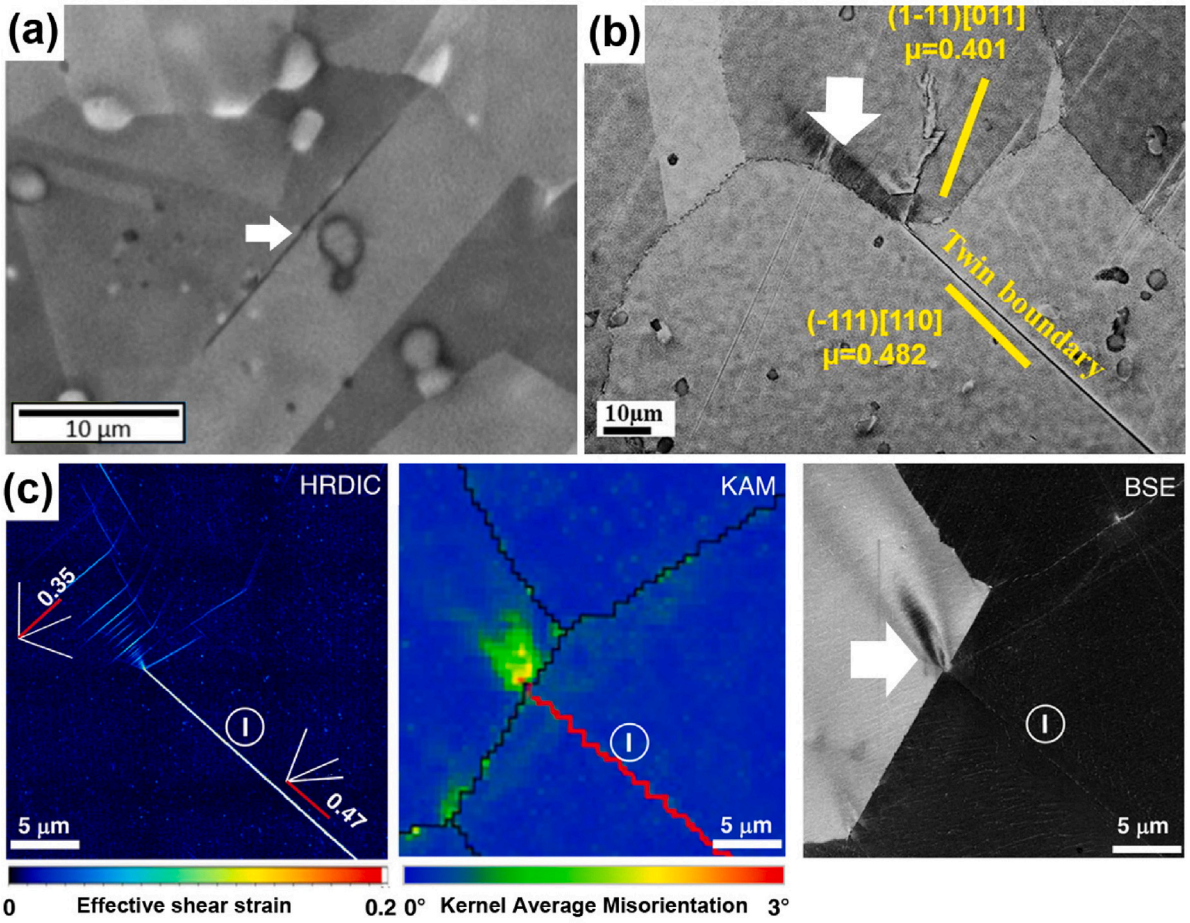

Fig. 1. Intense slip localization and early stage of crack nucleation in nickel-based superalloys. (a) Fatigue crack nucleation is observed at the surface in the middle of a grain [26]. (b) Crack nucleation occurs within a region of intense micro-strain gradients referred to as a microvolume [27,28]. (c) Microvolume originating from intense slip near and parallel to coherent twin boundary [24]. HRDIC, KAM, and BSE refer to high-resolution digital image correlation, kernel average misorientation, and backscatter electron, respectively. Panel adapted from Ref. [24,26,27] with permission from Nature, Elsevier, and Springer.

exhibit intense slip localization and slip irreversibility do not always lead to crack nucleation during cyclic loading [29]. This suggests that additional conditions might be necessary to trigger crack nucleation near CTBs, which have yet to be identified. Some research directions have been proposed based on observations related to crack nucleation. It has been reported that fatigue cracks near CTBs can nucleate at the surface either within the interior of the grain or in the vicinity of the intersection between the twin boundary and grain boundary of one of the neighboring grains [26–28,30–33], as illustrated in Fig. 1(a and b), respectively. Interestingly, in the latter case, a localized region exhibiting intense micro-strain, referred to as a microvolume [27,28], is observed in the neighboring grain, which seems to play a crucial role in triggering crack nucleation. These microvolumes form during the initial cycle as a result of the impingement of intense slip events [24,34,35], as shown in Fig. 1(c). Conversely, when the crack initiates at the surface in the interior of the grain, as depicted in Fig. 1(a), it is associated with the classic mechanism of intrusion–extrusion [6,36].

Further research is needed to explore and fully understand the specific conditions that control crack nucleation near CTBs and the role of microvolumes and extrusion–intrusion in this process. The present study addresses this knowledge gap by identifying the conditions and mechanisms responsible for crack nucleation near CTBs. The study focuses on the two observed mechanisms that contribute to crack nucleation near CTBs: microvolume and intrusion–extrusion. Tension–tension fatigue tests are conducted to achieve this goal, and slip irreversibility, and its evolution during cycling (slip accumulation), are carefully measured during the early cycling stage until crack nucleation occurs. By doing so, the configurations within the microstructure that promote slip accumulation and ultimately lead to crack nucleation are determined. Additionally, the article delves into the micro-mechanisms involved in crack nucleation and explores how the underlying microstructure influences them.

2. Experiments and materials

2.1. Material

The mechanical specimens were extracted from a wrought polycrystalline nickel-based superalloy Inconel 718 block. Thermal processing followed with a solution annealing step, 30 min at 1050 °C, followed by water quench. Afterwards, the material underwent precipitation hardening, by 8 h at 720 °C followed by 8 h at 620 °C. The microstructure of the material consists of crystallographic grains with an average grain size of approximately 60 µm, containing annealing twin boundaries, a high γ''-phase content, and a δ-phase content of a few percent. Non-metallic inclusions such as niobium-rich carbides, titanium-rich nitrides, and carbo-nitrides are present and sparsely distributed throughout the specimen. The nominal composition of the Inconel 718 is Ni - 0.56%Al - 17.31%Fe - 0.14%Co - 18.0%Cr - 5.4%Nb - 1.00%Ti - 0.023%C - 0.0062%N (wt%). The 0.2% offset yield strength was measured to be 979 MPa.

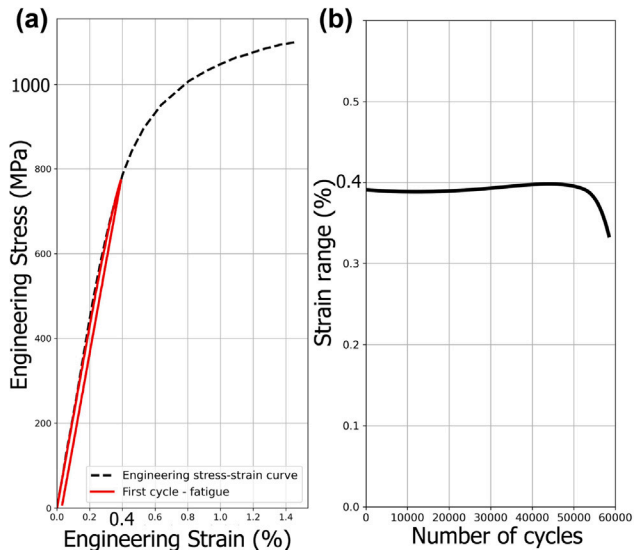

Fig. 2. (a) Engineering stress–strain curve of the investigated nickel-based superalloy. Initial cycle for the fatigue test performed at maximum applied stress of 785 MPa. (b) Associated strain range evolution as a function of the number of cycles during fatigue. Fatigue tests are performed in stress control at a near-zero ratio.

2.2. Mechanical testing

Tensile testing was performed at room temperature at a quasi-static strain rate using a custom in-situ ±5000 N stage within a ThermoFisher Helios microscope on a flat dogbone-shaped specimen with a gauge section of 1 × 3 mm^2. The tensile specimen was cut by wire electrical discharge machining, mechanically mirror polished using abrasive papers and diamond suspensions, and chemo-mechanically polished using a suspension of 0.04 μm colloidal silica particles. The tensile test was interrupted at macroscopic plastic strain levels of 0.8% and 1.26% to collect high-resolution images for digital image correlation measurements. The macroscopic strain was measured in situ using fiducial markers at both gauge length ends. The engineering stress–strain curve is provided in Fig. 2(a).

Cyclic tests were carried out using an Instron load frame with square-section specimens (cross-section of 3 mm^2) prepared like those used for tensile testing. The fatigue tests were conducted in stress control mode, employing a haversine waveform with a near-zero ratio (tension–tension) and a frequency of 1 Hz. Two applied maximum stresses with values of 835 and 785 MPa (below yield strength) were utilized. These testing conditions yielded a fatigue life of approximately 20 000 and 60 000 cycles, respectively, and a constant strain range during cycling as shown in Fig. 2(b) for maximum applied stress at 785 MPa. Interrupted fatigue tests were performed at specific intervals, specifically after 1, 2, 500, 10 000, 18 000, and 20 000 cycles.

2.3. Microscopy

Scanning electron imaging (secondary electron) for high-resolution digital image correlation (HR-DIC) was performed in an FEI Helios 600i Dual Beam SEM/FIB. Secondary electron image acquisition was conducted over an area of 988.5 × 1197 $μm^2$. The imaged area was an 8 × 7 grid pattern with a 10% overlap between neighboring images. The secondary electron imaging was performed at an accelerating voltage of 15 kV, a current of 0.69 nA (probe size of less than 10 nm), an image dwell time of 10 μs, a horizontal field width of 138 μm, at a working distance of 4 mm, and a pixel resolution of 6144 px × 4096 px. Secondary electron images were also used to identify crack nucleation. In addition, backscatter electron (BSE) images were acquired in an FEI Helios 600i Dual Beam SEM/FIB using an annular detector with a high-angle collection. These are utilized to identify areas with intense lattice rotation but were not employed for HR-DIC.

Finally, an FEI Helios 600i Dual Beam SEM/FIB was used to extract site-specific transmission electron microscope (TEM) foils. The foils were imaged in the scanning transmission electron microscopy (STEM) mode with a Talos TEM operated at 200 kV and equipped with a 4k × 4k Ceta™ 16 M camera.

2.4. High-resolution digital image correlation and electron backscatter diffraction

Before deformation, a speckle pattern consisting of 60 nm gold nanoparticles was applied to the sample surface using the method described by Montgomery et al. [37]. High-resolution digital image correlation (HR-DIC) was performed after unloading the specimen. The scanning electron microscope (SEM) images, with dimensions of 6144 px × 4096 px, were divided into subsets of 31 px × 31 px (equivalent to 696 nm × 696 nm) with a 3 px (equivalent to 67 nm) step size. The effective strain, ϵ_f, as defined in Ref. [38,39], was calculated at each point. Additionally, the Heaviside-DIC method, as described in Ref. [9,40], was utilized to calculate the in-plane slip amplitude. During mechanical loading, the investigated nickel-based superalloys undergo non-reversible plasticity in the form of slip bands. Local in-plane displacements occur within the material between both sides of the slip trace, and an amplitude characterizes these displacements. The in-plane slip amplitude represents the physical displacement in the plane of the surface resulting from a slip event between the material on the "left" and "right" sides of the slip trace. It is directly related to the number of dislocations, involved in a slip plane, that emerge at the surface [9,14]. In-plane displacement data includes two components, unlike the single-component out-of-plane displacement. A previous statistical study [12] has compared results from in-plane to out-of-plane displacements and found consistent results.

Conventional electron backscatter diffraction (EBSD) measurements were performed at 70° tilt using a step size of 1 μm, square grid collection, 200 frame per second acquisition, an accelerating voltage of 30 kV and a current of 2.6 nA before deformation on the region investigated by HR-DIC. EBSD was performed on a Thermo Scios2 Dual-Beam using a Hikari Super EBSD detector. EBSD maps were adjusted by distortion to match HR-DIC with pixel resolution using the method described in Ref. [41]. High-resolution electron backscatter diffraction (HR-EBSD) patterns were collected after deformation as well, using the above system. The patterns were obtained with a pixel resolution of 640 × 480 without binning (1 × 1). The pattern are collected at an accelerating voltage of 20 kV and a current of 2.6 nA as recommended in Ref. [42], with a step size of 0.1 μm at 70° tilt and a collection time of 200 ms, i.e., 5 frames per second. A cross-correlation approach was employed to evaluate local elastic strain/stress fields, utilizing the openly available OpenXY software [43,44]. This approach [45–47] enables the assessment of small crystalline lattice distortions and rotations from the EBSD patterns acquired in a deformed crystalline material. It has been successfully used to study micro-strain induced by slip impingement [28,48]. For each grain in the polycrystalline material, all the EBSD patterns are compared to a reference pattern, for which a rotation tolerance limits the misorientation between reference and experimental patterns, obtained from a "non-deformed" zone, located in the grain interior for the present study. The outcome of cross-correlation calculations applied to the patterns within a scanned area is a distortion matrix. The measured distortions are attributed to a combination of elastic strains and body rotations within the volume. It is possible to extract the strain tensor components from the distortion matrix. Furthermore, with the knowledge of the alloy's elastic constants [23], the elastic stress tensor can be computed using the strain tensor components. When substantial misorientation exists between the reference and analyzed patterns, cross-correlation analysis will result in

significant strain inaccuracy or error [49,50]. Given these considerations, the present study employs an exceedingly conservative threshold of 2° for maximum misorientation [49]. Any calculations derived from patterns exhibiting greater misorientation than 2° in comparison to the reference pattern are disregarded and referred to as "unindexed" in the present article. In addition, grain reference orientation deviation (GROD), characterized as the misorientation between the orientation at a specific location within a grain and the average orientation of that grain, was extracted from the EBSD measurements.

To avoid stress concentration effects from the specimen edges, all EBSD and HR-DIC measurements were conducted in the middle of the gauge length of the specimen.

2.5. A 3D microstructural perspective

To evaluate 3D microstructure effects, a multi-modal HR-DIC and 3D EBSD dataset, available publicly in Ref. [51], was used. The dataset contains high-resolution strain information at the surface of an identical nickel-based superalloy 718 specimen during monotonic deformation at 1.26% plastic deformation. In addition, the TriBeam system [52] was used to collect orientation fields in 3D over a half cubic millimeter volume. After mechanical testing, the specimen was unloaded, and surface EBSD measurements were performed on the same region of the specimen where the HR-DIC measurements were made. EBSD measurements were collected with a step size of 1 μm to form cubic voxels. The HR-DIC and EBSD measurements were correlated using the method in Ref. [53]. Individual slip traces were segmented from the HR-DIC data and indexed as individual features, using the iterative Hough transformation method presented in Ref. [54]. Slip bands were reconstructed in 3D using the location of the slip trace and crystallographic orientation data and spatially correlated with the 3D EBSD data. Details on the experimental procedure are provided elsewhere [51].

For the present study, grain reference orientation deviation is computed in 3D after deformation from the 3D dataset using the software Dream3D [55] and considering the average orientation of each 3D grain.

2.6. Numerical approach for resulting shearing from slip event

3D finite element method (FEM) calculations were performed to assess the local stress field that develops in the neighboring grain at the tip of the slip band associated with a shearing of the grain boundary. In the proposed approach, only one of the neighboring grains is explicitly meshed. As shown in Fig. 3, the grain in which the intense slip event has developed (grain 1) is not modeled, but the geometrical effect of the slip band on the grain boundary is considered using specific boundary conditions on neighboring grain (grain 2). Four of the six faces of the cuboid portion of the grain are constrained due to the surrounding microstructure. A displacement step is prescribed between the "left" and right" sides of the slip trace on the grain boundary face – modelized as a plane – in the direction of the identified slip system. Finally, free surface boundary conditions are considered on the top face of the grain. The constitutive law adopted for the modeled grain is the large strain formalism for elasticity and crystallographic slip developed in [56] and was introduced in the form of a user-defined mechanical material behavior (UMAT) subroutine implemented in ABAQUS/Standard. In this model, the slip activity per system is given by the slip rate and is defined using the following rate-dependent power-law flow rule

$$\dot{\gamma}^{\alpha} = \dot{\gamma}_0 \left| \frac{\tau^{(\alpha)}}{g^{(\alpha)}} \right|^{n} sgn(\tau^{(\alpha)}) \tag{1}$$

where $\dot{\gamma}_0$ is the reference slip rate, $\tau^{(\alpha)}$ and $g^{(\alpha)}$ correspond respectively to the resolved shear stress and the slip resistance on system α and n is the power-law exponent. Slip resistance for each slip system is assumed to undergo hardening according to

$$\dot{g}^{(\alpha)} = \sum_{\beta=1}^{N_s} h_{\alpha\beta} |\dot{\gamma}^{\beta}| \qquad g^{(\alpha)} = g_0, \{\alpha = 1, \ldots, N_s\} \tag{2}$$

where $h_{\alpha\beta}$ is a slip interaction matrix describing both self and latent hardening. Table 1 in Ref. [22] lists the values of the constitutive model parameters which have been calibrated by fitting the simulated stress–strain response of a representative volume element to experimental tensile data. Values of elastic constants were obtained from the literature [57]. The crystallographic orientation of grain 1 and the 3D orientation of the slip trace are derived from EBSD measurements, and the orientation of the grain boundary plane is informed by focused ion beam (FIB) cross-section and SEM images. The resulting mesh of the performed FEM simulation consists of approximately 1 million, 10-noded tetrahedral elements (C3D10).

3. Results

3.1. Cyclic slip accumulation and crack nucleation

HR-DIC measurements were performed during fatigue loading (tension–tension) and referenced to the initial deformation state. Consequently, the evolution of each slip event can be obtained during cycling. The effective strain and associated in-plane slip amplitude of a reduced region of interest are displayed in Fig. 4 after 2, 10 000, and 18 000 cycles. The associated EBSD map of the investigated region is provided in Fig. 4(c). The concentrated strain bands in Fig. 4(a, b) are evidence of slip. Relative evolution of the effective strain is observed between 2 and 10 000 cycles. While few additional slip events are reported after 10 000 cycles, the in-plane amplitude of slip events present after 2 cycles does not evolve significantly between 2 and 10 000 cycles, except for just a few slip events (see red arrows in Fig. 4(d and e). At 18 000 cycles, cracks were observed in the BSE images in the investigated region indicated by white arrows in Fig. 4(f); no crack was observed before 18 000 cycles. As reported in the literature for Alloy 718 [24] and other nickel-based superalloys [26,58], all cracks were observed near and parallel to CTBs under the applied loading conditions. It is essential to mention that the in-plane slip amplitude data obtained after 18 000 cycles, where cracks are present, represent not solely the local displacement induced by slip, but also the local displacement (crack opening [59]) induced by a crack when present.

A dataset containing approximately 500 slip events was extracted from the overall investigated region during fatigue loading. These slip events were organized into three categories: (i) slip events that form near and parallel to CTBs identified as crack nucleation sites; slip events occurring within a distance of less than 1 μm from CTBs were considered for this category; (ii) slip events that form near and parallel to CTBs but are not observed to be crack nucleation sites; (iii) the remaining slip events that are not near and parallel to CTBs. The slip events falling into the first and second categories are designated as being in "parallel slip configuration", as previously defined in the literature [19]. The maximum in-plane slip amplitudes of these slip events are depicted in Fig. 5 after 2, 500, 10 000, and 18 000 cycles. The maximum slip amplitude refers to the maximum value of the in-plane slip along the slip event, often observed near the middle of the slip event. To be noted, in Fig. 5(a), the in-plane maximum amplitude reported after 18 000 cycles for the slip events in the parallel slip configuration, which eventually led to crack nucleation, actually represents the displacement induced by the crack (i.e., crack opening). Violin plots are employed to visualize the distribution of the in-plane slip amplitudes, and horizontal dashed lines mark the averages of these distributions.

Slip events categorized as being in the "other configuration" display a relatively low initial maximum in-plane slip amplitude, and

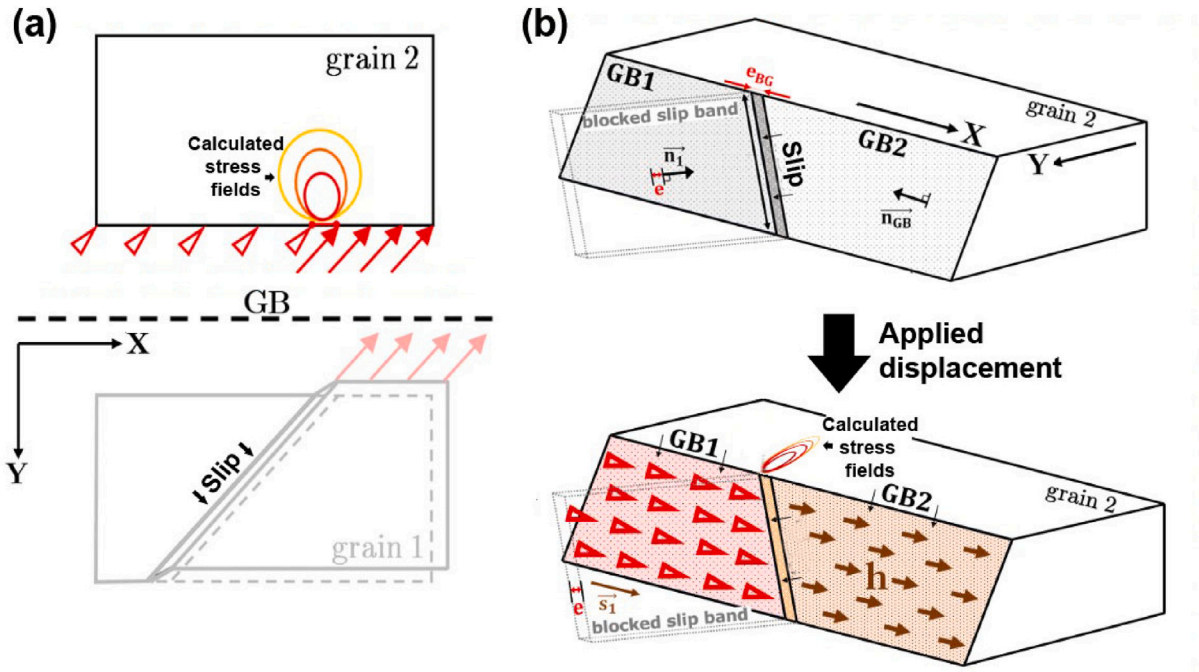

Fig. 3. Geometry and boundary conditions associated with the proposed model for simulation of local stress field associated with grain boundary shearing induced by a slip event. (a) representation in 2D; specimen surface. (b) representation in 3D. The model considers a shearing induced by a slip event near and parallel to a coherent twin boundary (grain 1) and calculates the stress field induced in the neighboring grain labeled "grain 2". GB1 and GB2 are the grain boundaries between grain 2 and grain 1. A displacement of one part of the GB2 simulates the shearing of the grain boundary GB2. The distance denoted as "e" represents the amplitude of the displacement caused by slip, and the vector $\vec{s}_1$ indicates its direction, as experimentally obtained through High-Resolution Digital Image Correlation measurements. Vector $\vec{n}_1$ indicates the normal of the active slip plane. Vector $\vec{n_G}B$ indicates the normal of the grain boundary between grain 1 and 2, while h indicates the amplitude of the applied displacement.

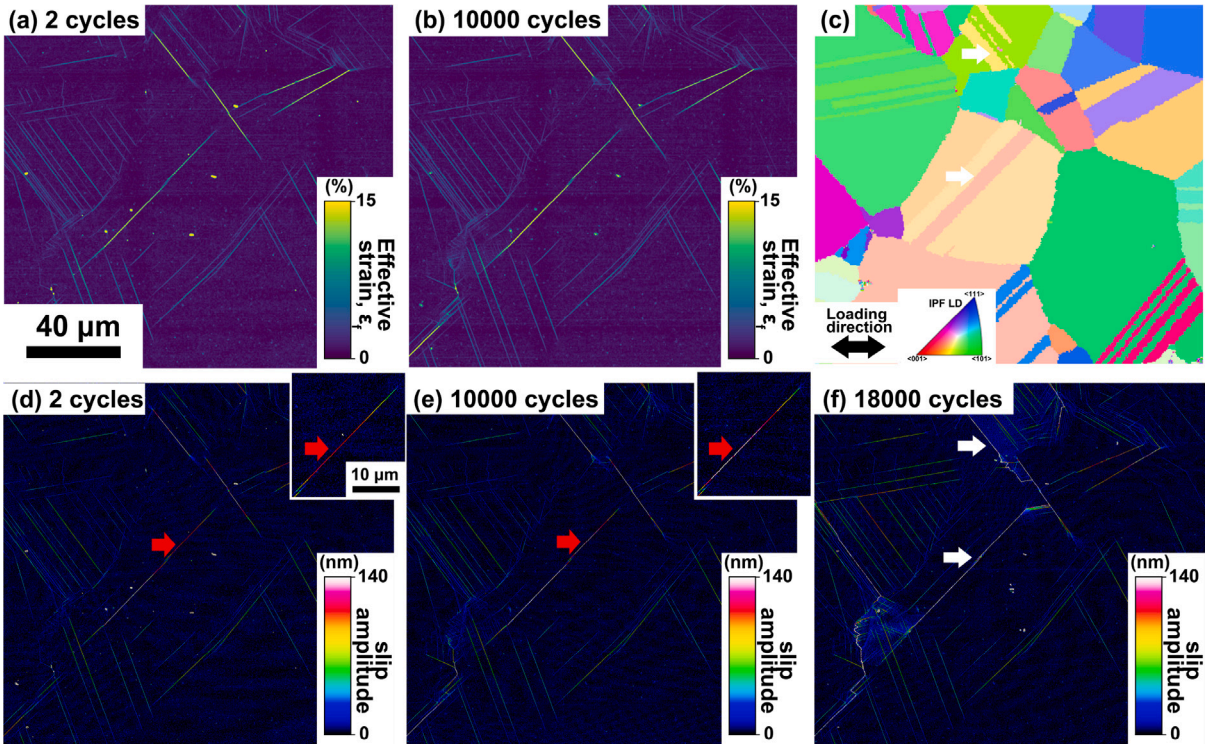

Fig. 4. Cyclic slip accumulation during fatigue testing. (a–b) The effective strain maps of a region of interest after 2 and 10 000 cycles. (c) Associated EBSD map. (d–f) Associated slip amplitude maps after 2, 10 000, and 18 000 cycles. The white arrows indicate the location of observed cracks. (For interpretation of the references to color in this figure legend, the reader is referred to the web version of this article.)

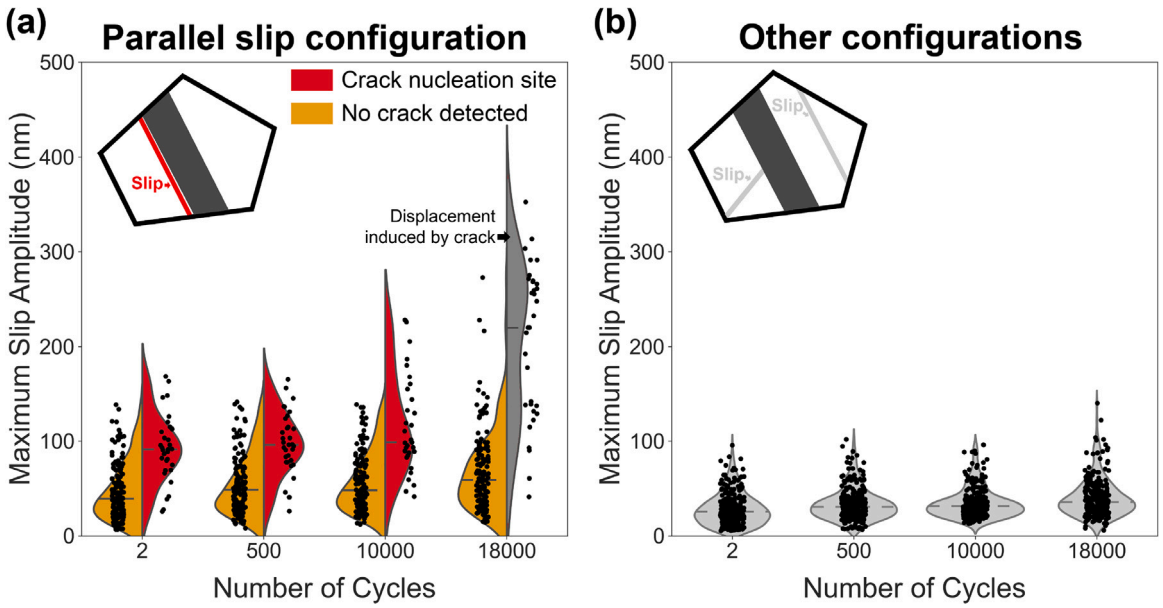

Fig. 5. Distribution of the maximum slip amplitude for each single slip event after 2, 500, 10 000, and 18 000 cycles. (a) slip events in parallel slip configuration [19] i.e., parallel and near CTBs. The right (red) and left (orange) distributions correspond to slip events that lead to crack nucleation or not, respectively. (b) Maximum slip amplitude distribution for the slip events not in parallel slip configuration. The in-plane slip amplitude data obtained after 18 000 cycles, where cracks are present, represent the local displacement (crack opening) induced by the crack. (For interpretation of the references to color in this figure legend, the reader is referred to the web version of this article.)

on average, there is no significant increase in the maximum in-plane slip amplitude observed during cycling. Similarly, for slip events categorized under the "parallel slip configuration", surprisingly, a similar observation is made. On average, the maximum in-plane slip amplitude does not show significant evolution during cycling up to 10 000 cycles, even for slip events that eventually lead to crack nucleation. The only noticeable difference observed between slip events in the parallel slip configuration that nucleated a crack and those that did not is that the maximum in-plane slip amplitude of the events leading to crack nucleation is initially higher compared to the events in the parallel slip configuration that do not lead to crack nucleation.

Fig. 6 presents the increase in maximum in-plane slip amplitude during cycling, expressed as a percentage difference between the maximum slip amplitude after 10 000 cycles and the initial two cycles. This parameter is referred to as "slip accumulation" as it represents the slip intensity accumulation that occurs during cycling, starting after the initial plastic deformation (initial cycles). The slip accumulation is provided in Fig. 6 as a function of the maximum slip amplitude. Each point in Fig. 6 corresponds to a single slip event, and they are categorized as previously described in Fig. 5. On average, very little slip accumulation is observed during cycling, regardless of the category considered. Additionally, no specific trend is observed among the slip events, as some display significantly different values in slip accumulation. Remarkably, for the slip events that eventually lead to crack nucleation, there is a mix of results: some exhibit intense slip accumulation, while others display negative slip accumulation, indicating a decrease in the maximum in-plane slip amplitude during cycling.

Fig. 7(a–d; e–h) presents two examples of slip events that led to crack nucleation, displaying negative and positive values of slip accumulation, respectively. The in-plane slip amplitude after 2, 10 000, and 18 000 cycles is shown in Fig. 7(b, c, and d) for the slip event displaying a negative value of slip accumulation. At 18 000 cycles, a crack was detected in the BSE images along a CTB, as evidenced by the intense in-plane displacement in Fig. 7(d). However, no cracks were detected at 10 000 cycles. Interestingly, the in-plane slip amplitude along the profile of the slip event leading to crack nucleation decreases significantly between 2 and 10 000 cycles. The second example of a slip event is displayed in Fig. 7(f, g, and h), and its slip amplitude

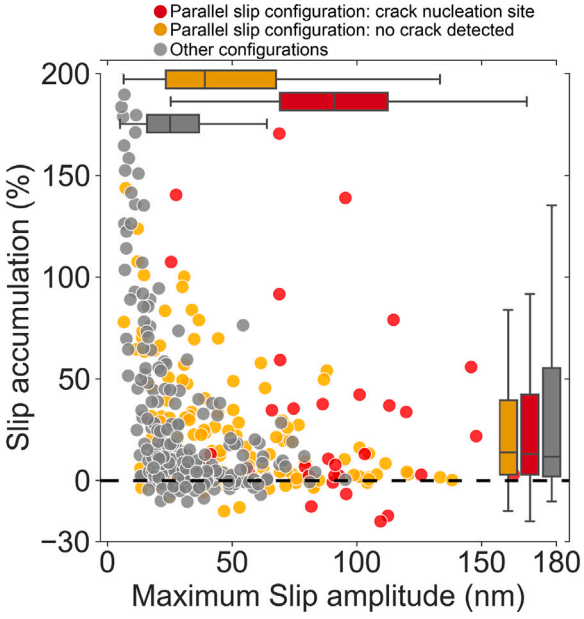

Fig. 6. Slip accumulation after 10 000 cycles, defined as the difference between the maximum slip amplitude after 10 000 cycles and the maximum slip amplitude after 2 cycles. The slip events are then classified based on whether they are in a parallel slip configuration and nucleate a crack.

is provided after 2, 500, and 10 000 cycles. No cracks were detected after 10 000 cycles. In both examples, it is evident that the slip events leading to crack nucleation are constrained within a crystallographic grain. Interestingly, significant plastic activity, before crack nucleation, is observed at the intersection of the slip events and the grain boundary of the neighboring grain, as shown in the insert in Fig. 7(h).

Fig. 8(a) presents the effective strain, ϵ_f, along the profile shown in Fig. 7(a) after 2, 500, 10 000, and 18 000 cycles. The analyzed slip event corresponds to the one displayed in Fig. 7(a–d), exhibiting

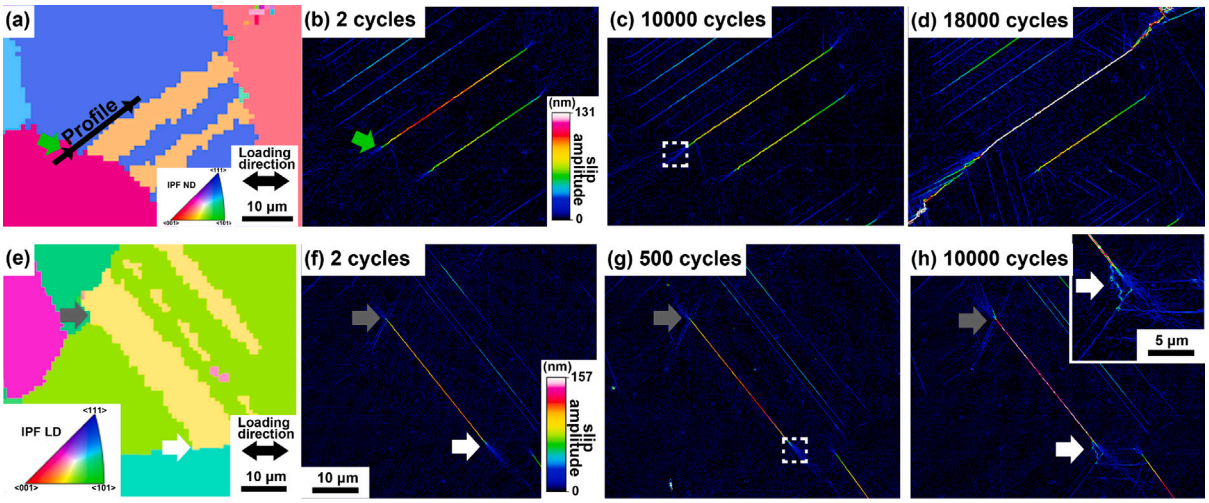

Fig. 7. Two examples (a–d and e–h) of slip events that led to crack nucleation along and near CTBs. EBSD maps are provided in (a) and (e). The associated in-plane slip amplitude after 2, 500, 10 000, and 18 000 cycles are provided in (b–d, f–h). Cracks were only detected after 18 000 cycles. (For interpretation of the references to color in this figure legend, the reader is referred to the web version of this article.)

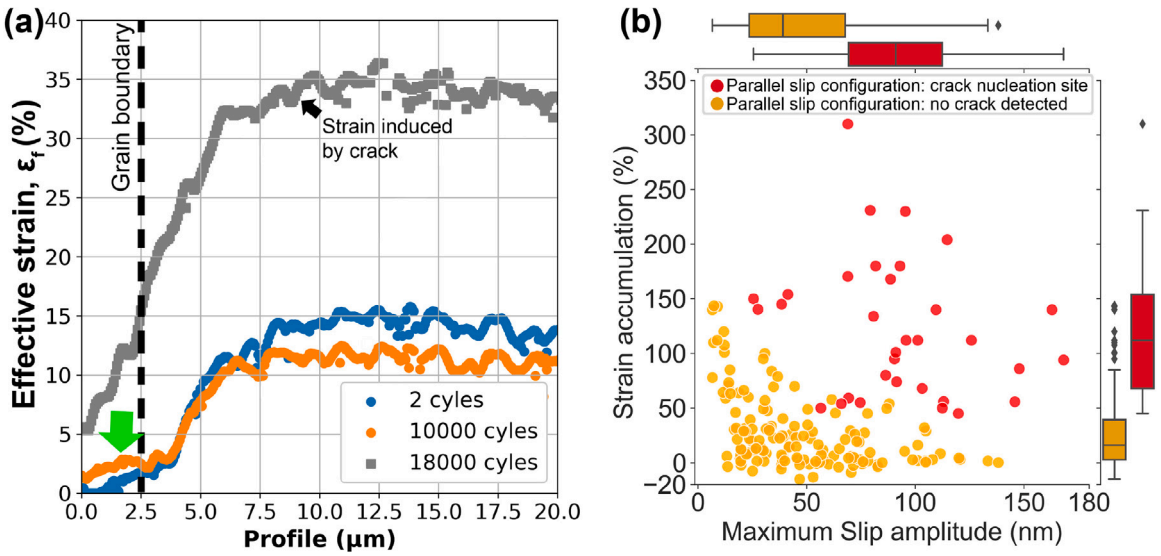

Fig. 8. (a) Effective strain along the profile depicted in Fig. 7(a) after 2, 500, 10 000, and 18 000 cycles. (b) Average effective strain in a reduced region at the intersection of slip events in parallel slip configuration, whether associated with a crack or not, and the neighboring grain boundary. Each point is associated to a slip event that impinges a grain boundary.

negative slip accumulation and leading to crack nucleation after 18 000 cycles. The effective strain becomes significant after 18 000 cycles, indicating the presence of a crack. It is observed that the effective strain decreases along the slip event between 2 and 10 000 cycles, which aligns with the previously observed decrease in maximum in-plane slip amplitude during that period. Interestingly, near the intersection of the slip event with the grain boundary of the neighboring grain (indicated by the black dashed line in Fig. 8(a) and green arrow in Figs. 7(a and b) and 8(a)), an increase in effective strain in the neighboring grain is observed between 2 and 10 000 cycles, suggesting a local increase in plastic activity during cycling. Fig. 8(b) displays the evolution between 2 and 10 000 cycles of the average effective strain in a reduced region at the termination of all slip events in a parallel slip configuration, whether associated with a crack or not, and in the neighboring grain. The dashed white boxes in Fig. 7(c and g) illustrate examples of the regions under investigation. The effective strain accumulation is plotted as a function of the maximum slip intensity of the associated slip event. Noticeably, effective strain is rising considerably throughout the cycling process in the region where crack nucleation occurred. In contrast, regions where crack nucleation did not occur, systematically demonstrate a lower accumulation of effective strain.

3.2. Microvolumes and crack nucleation

As the preceding section shows, significant plastic activity occurs at the intersection of intense slip bands that lead to crack nucleation and the neighboring grain boundary. The in-plane slip amplitude map at one of these intersections after 10 000 cycles is depicted in Fig. 9(a), and the complete map can be found in Fig. 7(h). The associated HR-DIC SEM images after 10 000 and 18 000 cycles are provided in Fig. 9(b and c), respectively. Notably, localized and short slip events are observed in the neighboring grain, as indicated by the white arrow in Fig. 9(a,b,c). Interestingly, these slip events exhibit typical material extrusion patterns known to be the origin of crack nucleation during fatigue at a ratio of −1 (tension–compression) [58,60]. However, such material extrusion is not observed along the intense slip band in the parallel slip configuration, suggesting that the origin of crack nucleation occurs in a localized region within the neighboring grain.

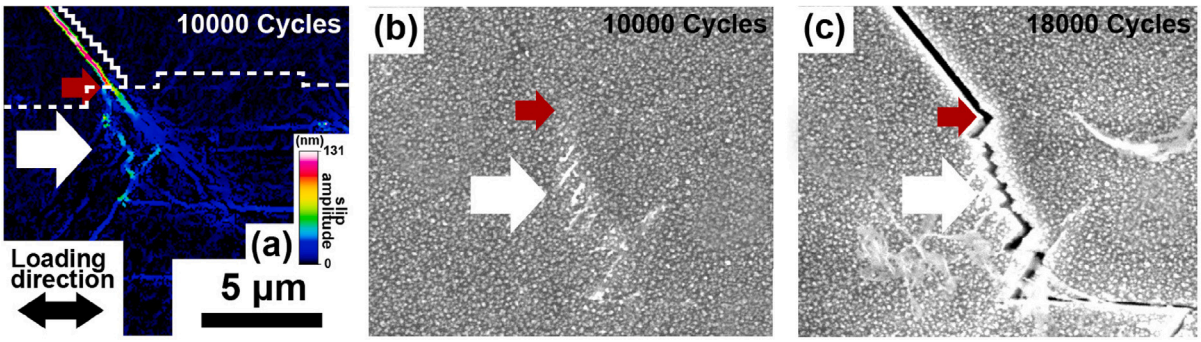

Fig. 9. (a) In-plane slip amplitude map after 10 000 cycles showing slip activity in a localized region in the neighboring grain where an intense slip band impinged the grain boundary. A dashed white line displays the grain boundary. (b–c) Associated HR-DIC images after 10 000 and 18 000 cycles, respectively, showing intrusion/extrusion patterns and resulting crack nucleation.

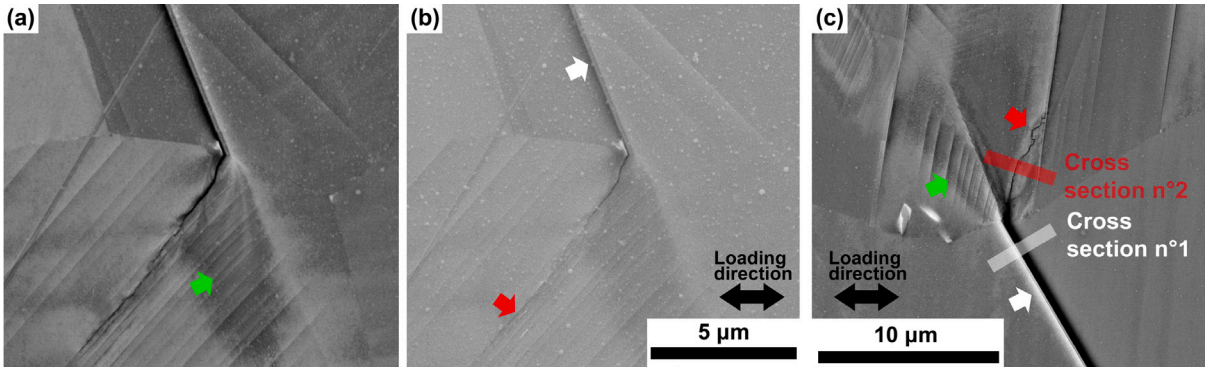

Fig. 10. (a,b) BSE and SE images of incipient crack nucleation after 20 000 cycles. Material extrusion, shown by the red arrow, is observed in (b). (c) Another example of incipient crack nucleation. Crack nucleation occurred on the right of a microvolume. (For interpretation of the references to color in this figure legend, the reader is referred to the web version of this article.)

Fatigue tests were conducted with numerous interruptions, in order for BSE and SE images to be captured between each interruption to detect the incipient crack nucleation. Within an investigated 2 mm^2 area, incipient crack nucleations were systematically observed in the vicinity of the impingement of a slip band on a grain boundary in the neighboring grain, as described in Fig. 9 and demonstrated in Fig. 10. Interestingly, material extrusion, indicated by the red arrow in Fig. 10(b), was observed. Additionally, regions of intense plasticity with BSE contrast (highlighted by the green arrows in Fig. 10), indicating significant lattice rotation, were observed in the neighboring grains where a slip band impinged. These features, sparsely reported in the literature, are referred to as microvolumes [27,28]. Microvolumes were consistently observed in all investigated cracks after an initial cycle.

To confirm the presence of incipient cracks in the neighboring grains, but not along the intense slip events parallel to and near CTBs, TEM foils were extracted after 20 000 cycles from the neighboring grains and close to CTBs. TEM images of these foils, corresponding to the areas marked by transparent white and red rectangles in Fig. 10(c), are showcased in Fig. 11. A notable slip step is evident near the CTB and running parallel to it, with signs of slip taking place along and offset the CTB. Yet, no cracks are discernible, as shown in Fig. 11(a). On the other hand, the TEM image from the neighboring grain exhibits a crack, highlighted by the red arrow in Fig. 11(b). Interestingly, a microvolume is observed within the bulk, indicated by the green arrow in Fig. 11(b), which might originate from an intense slip event along a bulk CTB.

3.3. Origin of the microvolumes

Fig. 12(a) shows the effective strain map, and Fig. 12(b) displays the in-plane slip amplitude map after a tensile test at 0.8% plastic deformation. A region with a microvolume is observed, associated with the impingement of a slip event in the parallel slip configuration with a grain boundary. The size of these microvolumes in the neighboring grain is observed to depend on the in-plane slip amplitude of the intense slip events that generated them. Notably, the BSE images in Fig. 12(c) and (d) reveal a physical shearing of the grain boundary caused by the intense slip events, which is the origin of the microvolumes.

Following the tensile test, microvolumes were investigated using HR-EBSD measurements, as detailed in Section 2.4. Two examples are shown in Fig. 13. Remarkable lattice rotation is evident within the microvolumes and their surroundings, as depicted in the GROD maps of Fig. 13(b and e). The magnitude of lattice rotation within these microvolumes is substantial, often exceeding 10°. The most notable lattice rotations are concentrated near the grain boundary where the grain boundary shearing occurred. Computed elastic σ_{11} stress maps (aligned with the loading direction) derived from the HR-EBSD data are illustrated in Fig. 13(c and f). While low elastic stresses are reported for the microvolume in Fig. 13(a,b), it becomes apparent that the intense microvolume shown in Fig. 13(d,e) coincides with pronounced elastic stress variations. Interestingly, negative stress values are observed in the vicinity (indicated by green arrows) of the microvolume.

3.4. A 3D perspective

The investigated multi-modal 3D dataset combines high-resolution strain field information with the 3D microstructure after tensile deformation at 1.26% plastic deformation. The 3D location and intensity of slip events within the surface grains are also provided.

The GROD 3D data was extracted from the 3D microstructure. By applying a threshold on the GROD angle data, regions with values higher than 2° can be identified. Within the microstructure, micro-scale regions with significantly high GROD angle values are observed near

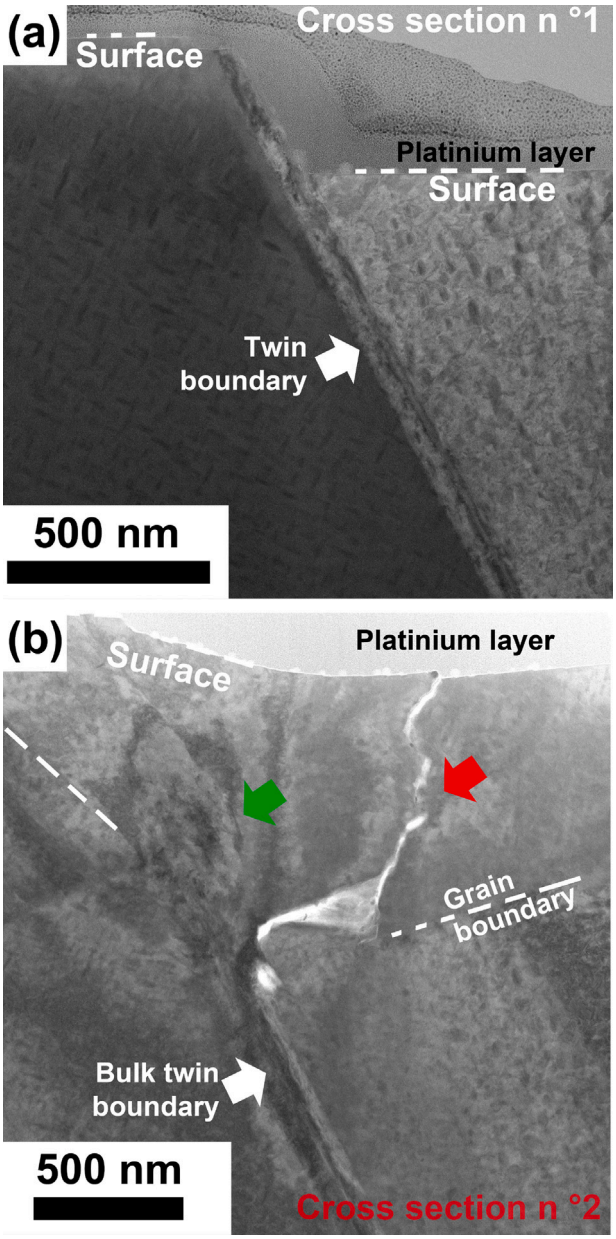

Fig. 11. TEM image of cross-sections extracted in a neighboring grain when an intense slip event impinged its boundary (a) and across a CTB where intense slip event developed. TEM foils were extracted after 20 000 cycles, where crack nucleation was observed. The locations of the foils are detailed in Fig. 10(c). (For interpretation of the references to color in this figure legend, the reader is referred to the web version of this article.)

grain boundaries at the free surface of the specimen (grain labeled S2 in Fig. 14(a)) and within the bulk (grain labeled B1 in Fig. 14(b)). The correlative measurements between HR-DIC and 3D microstructure enable the spatial registration of these micro-scale regions with slip events. It is observed that microvolumes with significantly high GROD angle values correlate with the impingement of intense slip events at grain boundaries (see slip event labeled 1 and 2 in Fig. 14(a and b), respectively). Supplementary materials provide additional examples in the form of videos. Interestingly, microvolumes are observed in both surface and bulk grains.

Intense slip events with a maximum in-plane slip amplitude greater than 50 nm were investigated. These slip events impinge grain boundaries between the grain where the slip event occurred and their neighboring surface and bulk grains, as shown in Fig. 14(a) for the labeled slip #1. Fig. 14(a) illustrates that a slip event can produce a microvolume in one neighboring grain while not in another. For all six investigated intense slip events, a set of m' factors was calculated between the active slip system of the slip event (identified by the H-DIC method, see Ref. [61]) and the slip system with the highest Schmid factor in the neighboring grains. The m' factor, introduced by Luster and Morris [62], was used to assess slip system alignment on both sides of the boundaries. It is calculated as the product of cosines between slip plane normals and between slip directions. Thus, m' = 1 indicates a perfect alignment between deformation systems on both sides of the grain boundaries. Subsequently, the thresholded GRODs in the neighboring grains were investigated to identify if the intense slip event developed a microvolume with significantly high GROD angle values where the slip event impinged the grain boundary. The maximum values of the GROD inside the microvolumes were extracted. Fig. 14(c) displays these values and associated m' factors as a function of the maximum in-plane slip intensity of the investigated slip events. A black dot indicates that no microvolume was detected. A horizontal dashed line represents a single slip event and has multiple measurement points (m' and highest value of the GROD) since the slip event impinges on multiple neighboring grains. It is observed that intense slip events may produce intense microvolumes (high values of GROD) when the m' factor is relatively low, indicating a scenario where slip transmission is not facilitated. Conversely, no microvolume is observed if the m' factor is high or the amplitude of the slip events is low.

4. Discussion

In metallic materials with a minimal amount of metallurgical defects, crack nucleation is closely tied to the grain structure and arises from an intrusion–extrusion mechanism associated with cyclic irreversibility [3,6,11]. During cyclic loading, the development of persistent slip bands or fatigue shear bands [3,5,63] creates intense cyclic slip irreversibility [11], leading to the formation of surface intrusion–extrusion patterns that intensify over cycling and eventually give rise to microcracks [60]. This phenomenon has been observed during low-cycle fatigue under a negative fatigue ratio (tension–compression) [60,64,65]. In polycrystalline nickel-based superalloys, these intrusion–extrusion patterns originate from the initial cycle, where "positive" surface steps are formed during tensile loading, and redistribution of slip at specific microstructure features occurs during compressive load resulting in "negative" surface steps [9]. This results in the intrusion–extrusion mechanism during the subsequent cycles [9], and ultimately, crack nucleation [21]. However, there are certain loading conditions where cracks do not nucleate at the surface of the specimen but rather internally, and the phenomenon of surface intrusion–extrusion cannot fully explain crack initiation. For instance, in the high cycle fatigue regime with low applied stress, cracks can nucleate internally and still be related to the grain structure [66]. Another condition where the intrusion–extrusion mechanism may be suppressed is during fatigue loading with a positive ratio (tension–tension), where "negative" slip steps are supposedly not produced. Furthermore, when examining nickel-based superalloys, crack nucleation is often associated with CTBs that experience intense slip localization during the initial cycle [58,67]. However, not all CTBs displaying initial intense slip localization lead to crack nucleation [29]. All of these observations suggest the existence of other critical mechanisms during cycling that drive crack nucleation.

4.1. Micro strain, slip accumulation, and crack nucleation

These considerations motivated the present study, which involves fatigue loading with a positive ratio (tension–tension), where extrusion–intrusion is hindered. Additionally, we purposefully applied a relatively low maximum stress to avoid significant ratcheting, thereby ensuring a consistent strain range throughout cycling. This approach was adopted

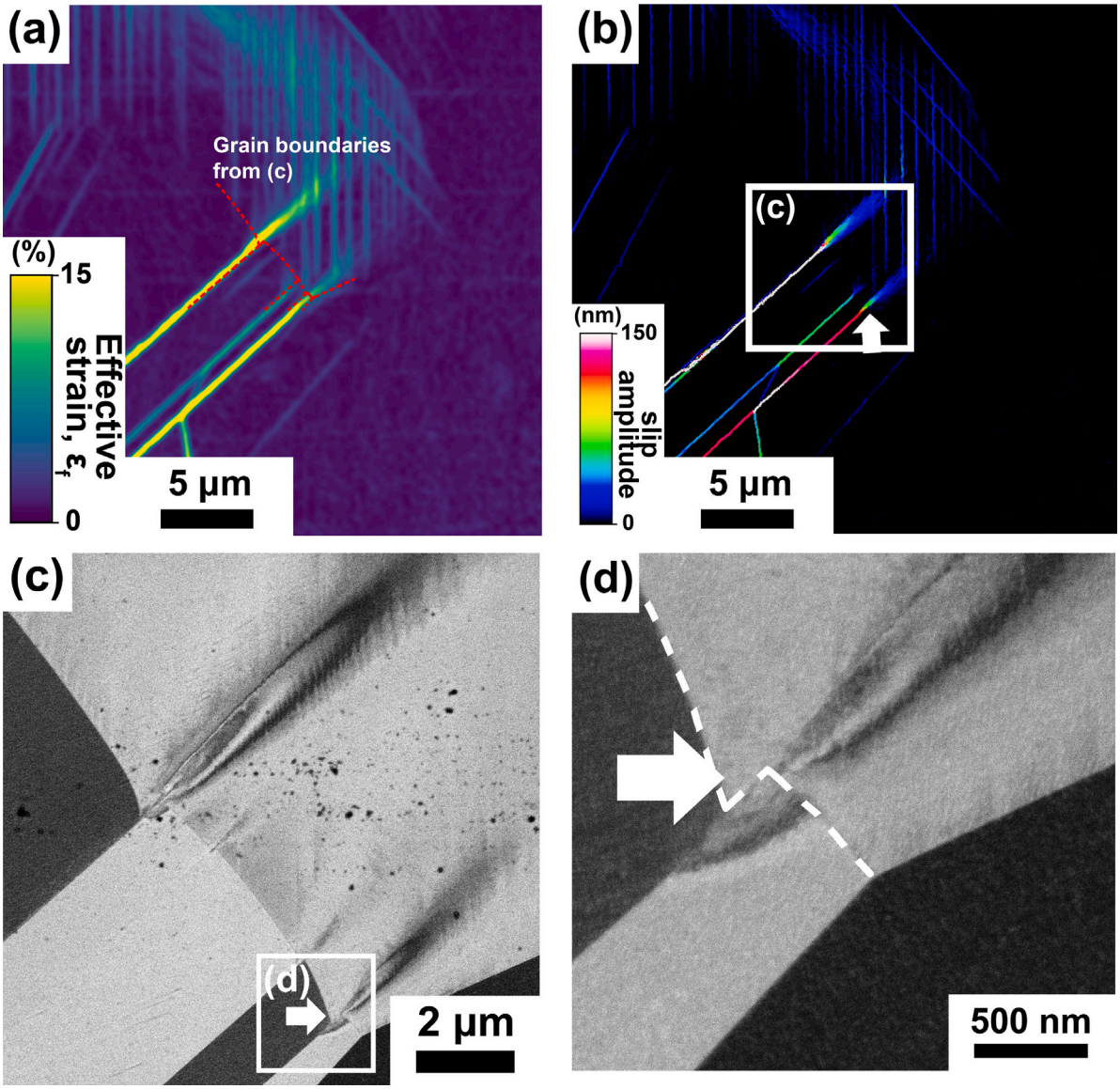

Fig. 12. (a,b) Effective strain and in-plane slip amplitude maps of a region of interest that display several microvolumes after an initial cycle. (c,d) Associated BSE images displaying the microvolumes. The intense contrast in the images indicates a change in crystallographic orientation. The red dashed lines in (a) are the grain boundaries identified in (c). The white dashed line in (d) indicates grain boundaries. (For interpretation of the references to color in this figure legend, the reader is referred to the web version of this article.)

to more readily highlight and analyze the critical deformation and damage mechanisms.

In Fig. 4, it is evident that the mechanism of slip redistribution observed during fatigue with a negative ratio (tension–compression) [9] is not observed during fatigue with a positive ratio. Specifically, single initial intense slip events develop near and parallel to CTBs during the initial cycle and persist throughout the cycling process; no additional slip events are observed nearby and parallel to these initial events, as is typically observed during fatigue with a negative ratio [9]. Moreover, the surface displacement produced by the initial slip events that eventually lead to crack nucleation does not consistently increase during cycling, as shown in Fig. 6. This indicates that the intensification of cyclic slip irreversibility along CTBs, which was observed to be a controlling mechanism during fatigue with a negative ratio, does not play the same role in crack nucleation under the current positive fatigue ratio. Interestingly, notable plastic activity evolution is observed in reduced regions within the neighboring grains where intense slip bands in parallel slip configuration impinge the grain boundaries. Fig. 8(b) displays the effective strain accumulation in these reduced regions, and it becomes evident that such strain accumulation is a controlling factor for crack nucleation. A combination of factors is observed to be necessary for crack nucleation: a highly intense slip event occurring near and parallel to the CTB and significant strain accumulation in the neighboring grain. Of particular interest, within these reduced regions of intense strain accumulation (shown in Fig. 9), material extrusion during cycling is observed, which is typically associated with fatigue at a negative ratio along intense slip events near and parallel to CTBs [58,60,68,69]. These regions appear to be the sites of incipient crack nucleation, as depicted in Fig. 10, and subsequent rapid crack propagation occurs along the intense slip events parallel and near the CTBs. Initially referred to as microvolumes, they were known to display intense lattice rotation and elastic strain [27,28], but are now observed to induce material extrusion during cycling resulting in crack nucleation.

4.2. Origin of microvolumes

The present study reveals that the intensity of microvolumes (effective strain and induced lattice rotation) is correlated with the intensity of the slip events that generated them. It is worth mentioning that

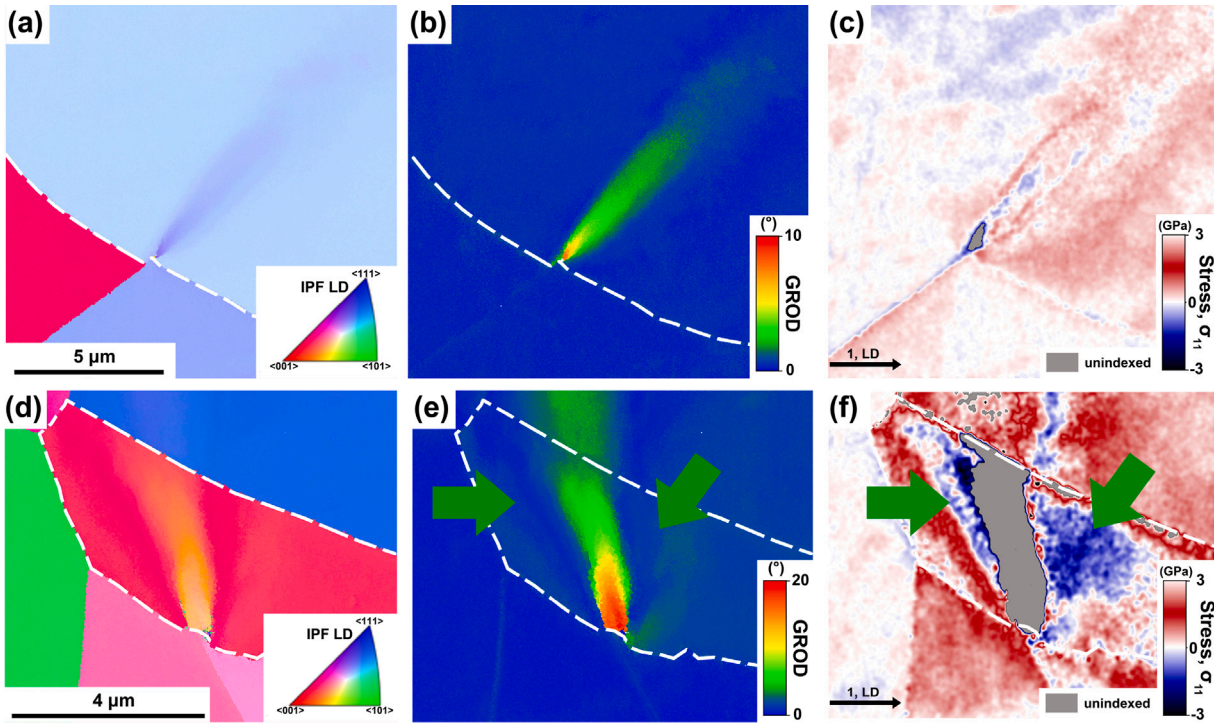

Fig. 13. (a,d) Inverse pole figure map along the loading direction of regions displaying microvolumes. (b,e) Associated GROD maps. (c,f) Associated stress maps were calculated using the cross-correlation approach from the HR-EBSD data. σ_{11} refers to the stress component along the loading direction. (For interpretation of the references to color in this figure legend, the reader is referred to the web version of this article.)

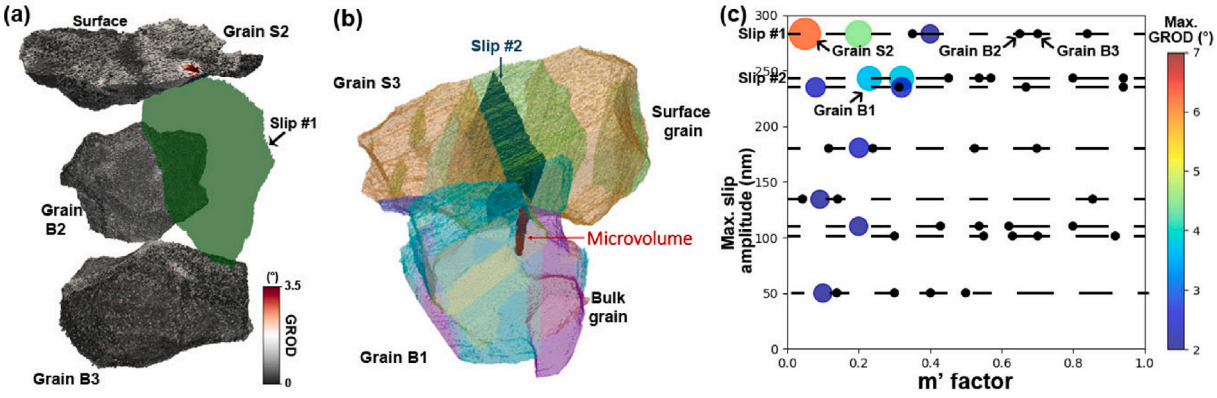

Fig. 14. Micro-strain gradients at the specimen surface and in the specimen bulk induced by intense slip events. Slip events of interest are represented by a transparent green plane and are impinging multiple grains. (a) 3D GROD map showing the presence of a microvolume in the grain labeled S2 and no microvolume in the other displayed grains labeled B2 and B3. (b) A microvolume is observed in a grain labeled B1 located in the bulk of the specimen. (c) Intensity of the microvolumes (maximum value of the GROD) for slip events of high slip amplitude. A dashed black line represents a slip event. The associated points represent the intensity of the microvolumes produced by the slip events in the neighboring grains. Black points indicate no microvolume. Each microvolume is displayed as a function of the m' factor associated with the grain in which the microvolume is observed. (For interpretation of the references to color in this figure legend, the reader is referred to the web version of this article.)

the slip intensity is related to the length of the slip bands as initially mentioned by Kim and Laird [21] and quantified in Ref. [58]. Furthermore, these microvolumes emerge after the initial cycle and originate from the shearing of the grain boundary where the intense slip events impinged, as illustrated in Fig. 12. Additionally, they occur when direct slip transmission is prevented, as observed in Fig. 12(b), and this is indicated by their dependence on the m' factor (see Fig. 14(c)). In configurations of non-slip transmissions, intense micro-strain/stress is observed in the neighboring grains due to dislocation pile-up [70–73]. However, the micro-strain observed in the present study significantly differs from that induced by dislocation pile-up. The lattice rotations observed are notably higher than that which is produced by dislocation pile-ups and these areas of lattice rotation extend over several micrometers [70,71,74]. Usually, when dislocation pile-up occurs, and applied stresses continue to rise, it leads to slip transfer, indirect transmission/dislocation source activation, or damage at grain boundaries [75]. Multiple failure theories have identified strain localization [76] and increases in strain energy due to a lack of slip transfer and dislocation pile-up as causes of crack nucleation [77–81]. Liu et al. [82] attempted to shed light on the competition between dislocation transmission and dislocation source activation; they associated the formation of microvolumes with micro-strain associated with dislocation pile-up, but did not envision other scenarios. It is evidenced in the present study that the initial pile-up of dislocations does not lead to slip transfer or

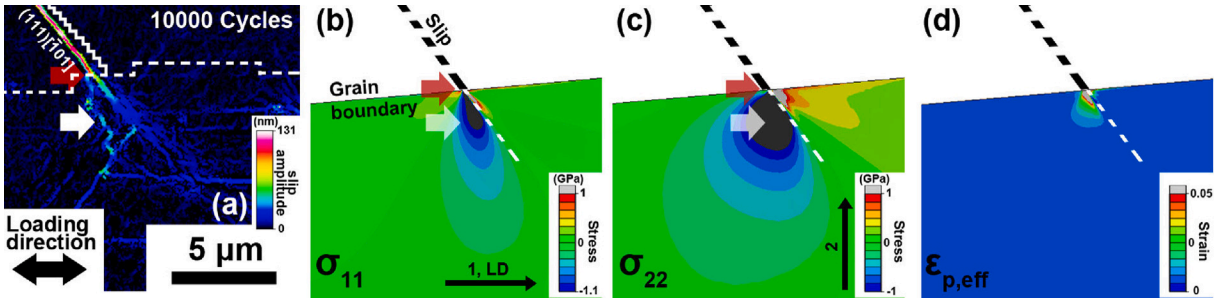

Fig. 15. (a) In-plane slip amplitude map after 10 000 cycles showing slip activity in a localized region in the neighboring grain where an intense slip band impinged the grain boundary. A dashed white line displays the grain boundary. (b–c) Associated stress maps were calculated using the numerical approach described in Section 2.6. σ_{11} and σ_{22} refers to the stress components along the loading direction and transverse direction. Dashed black lines display the slip band. (d) Associated effective plastic strain map. The effective plastic strain is calculated following the definition in ref. [86] with the Mises strain factor of 2/3.

indirect transmission/dislocation source activation; instead, it causes shearing of the grain boundaries.

The occurrence of microvolumes is closely associated with intense slip events [83], which explains why they are not commonly observed in other material systems with lower yield strength, where slip amplitudes are generally lower [12]. Furthermore, the activation of a microvolume originates from non-slip transfer, which is significantly influenced by the grain boundary energy [84], making it highly dependent on the specific material system.

From an analysis of Figs. 9 and 10, a surprising observation emerges: cracks tend not to nucleate in the main zone (highest lattice rotation intensity) of the microvolume, a phenomenon hypothesized in a previous study [28] (see Fig. 1(b)). The main zone generates high-tensile stresses, while some surrounding zones produce compressive stresses, as Fig. 13 shows. These regions of compressive stresses may be responsible for the classical intrusion–extrusion mechanism observed during fatigue, as shown in Fig. 9(b), explaining the occurrence of early surface crack nucleation during fatigue at a positive ratio.

To further validate the occurrence of negative stress regions induced by microvolumes, a numerical model was developed to assess the stress distribution associated with a microvolume. This analysis involves considering grain boundary shearing and conducting finite element analysis on the grain configuration in Fig. 7(e–h) and Fig. 9. The details of the model are provided in Section 2.6. By leveraging the Heaviside-DIC approach in conjunction with EBSD measurements, the parameters of shearing induced by the parallel slip configuration events can be determined [61]. The experimentally obtained slip displacement angle of 1.2° aligns closely with the theoretical prediction of 0.99° for the slip system $(111)[\bar{1}01]$, which also is the highest Schmid factor considering the macroscopic loading direction. The stresses resulting from this theoretical shearing are visualized in Fig. 15(b–c) using the proposed model. Strikingly, negative stresses emerge on the side of the microvolume with the presence of plastic deformation, as evidenced in Fig. 15(d), coinciding with the region where material extrusion was observed during cycling experiments. This computational analysis corroborates that negative stresses induced near microvolumes through grain boundary shearing represent zones of intense plastic irreversibility, thereby playing a significant role in crack nucleation. Compressive stresses induced by impingement of slip events were also observed in titanium and magnesium alloys [85], indicating that the observed mechanisms can also be present in other material systems.

In Fig. 11(b), we noted an additional microvolume within the bulk, which might contribute to crack initiation alongside the primary microvolume depicted in Fig. 10(c). This pairing of closely spaced microvolumes might generate a complex local stress field, inducing significant compressive stresses and early crack nucleation. The first two crack nucleation sites observed in the incremental fatigue test were also attributed to the merging of two microvolumes, as illustrated in Fig. 16, reinforcing the controlling role of microvolumes as the origin of crack nucleation at a positive ratio. What remains to be identified is the

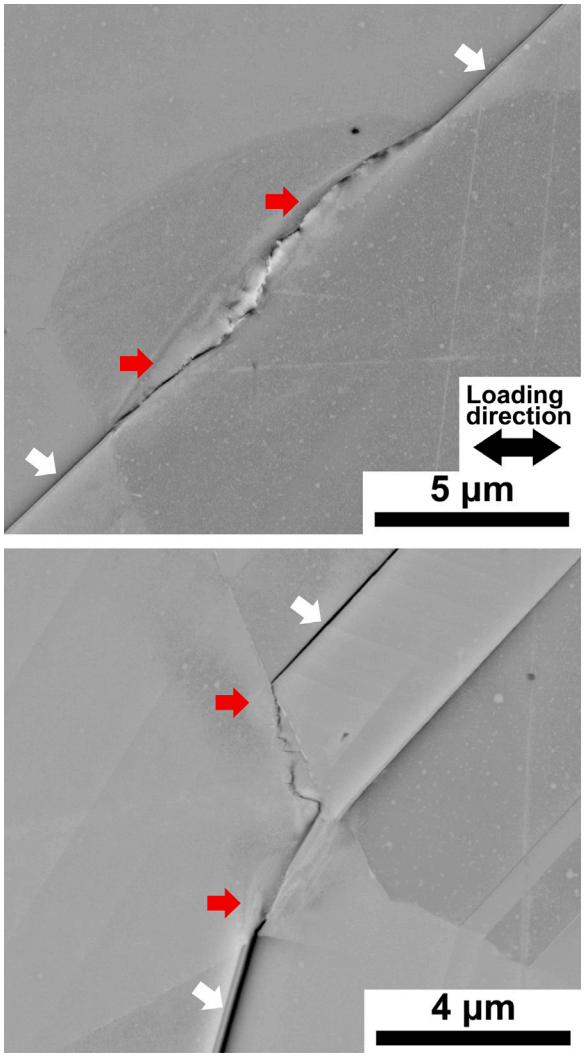

Fig. 16. First evidenced crack nucleation after 12 000 cycles. It involved a combination of microvolumes. White arrows indicate the presence of CTBs with intense slip localization in their vicinities. Red arrows indicate microvolumes. (For interpretation of the references to color in this figure legend, the reader is referred to the web version of this article.)

competing role of microvolume and conventional extrusion–intrusion mechanisms that occur near CTBs when specimens are subject to fatigue at a negative ratio, when crack nucleation seems either to occur along CTBs or at microvolumes (see Fig. 1). Furthermore, although the crystal plasticity numerical model and HR-EBSD measurements indicate the presence of negative stresses in regions near some microvolumes after the initial cycle, there remains a need to comprehend the evolution of these stresses during cycling. This necessitates the incorporation of a kinematic hardening law into the model and the continuous monitoring by HR-EBSD measurements during cycling. Additionally, it is crucial to gain insight into the origin of the observed local increase in effective strain within the microvolumes during cyclic loading. This increase is attributed to dislocation transmission from the main slip event to the microvolume, as evidenced by a decrease in in-plane amplitude for certain slip events. However, it is also worth considering the possibility of dislocation emission occurring from the microvolume itself during cycling.

5. Conclusions

Strain and slip irreversibility were investigated at the nanometer scale using high-resolution digital image correlation and high-resolution electron backscatter diffraction during tensile and cyclic loading. We highlight distinct deformation mechanisms that contribute to crack nucleation in the investigated nickel-based superalloy. The following conclusions are drawn.

- Intense slip events occur during the initial fatigue cycle, adopting a parallel slip configuration, which triggers shearing at grain boundaries. This phenomenon leads to the creation of microvolumes within adjacent grains.
- Microvolumes are distinguished by their intense plastic activity, accompanied by significant lattice rotation and positive and negative elastic stresses.
- The combination of negative elastic stress triggers extrusion of material during cycling, ultimately leading to crack nucleation.
- It is noteworthy that the cyclic slip accumulation near twin boundaries does not serve as a good predictor of crack nucleation. Some slip events are observed to reduce in intensity during cycling, while still leading to crack nucleation.
- The creation of microvolumes occurs at the surface and within the bulk in scenarios where intense slip bands impinge grain boundaries and slip transmission is hindered.

Declaration of competing interest

The authors declare that they have no known competing financial interests or personal relationships that could have appeared to influence the work reported in this paper.

Acknowledgments

RLB and JCS are grateful for financial support from the Energy & Biosciences Institute (EBI), through the EBI-Shell Program. DA and JCS acknowledge the National Science Foundation (NSF award #2234892) for financial support. This work was carried out in the Materials Research Laboratory Central Research Facilities, University of Illinois, and at the Advanced Materials Testing and Evaluation Laboratory, University of Illinois. Tresa M. Pollock, Marie Charpagne, and Irene J. Beyerlein are acknowledged for fruitful discussions. Patrick Villechaise is acknowledged for his support on HR-EBSD measurements. Stéphane Forsik and Carpenter Technology are acknowledged for providing the 718 material.

Appendix A. Supplementary data

Supplementary material related to this article can be found online at https://doi.org/10.1016/j.actamat.2024.119657.

References

[1] Johannes Schindelin, Ignacio Arganda-Carreras, Erwin Frise, Verena Kaynig, Mark Longair, Tobias Pietzsch, Stephan Preibisch, Curtis Rueden, Stephan Saalfeld, Benjamin Schmid, Jean-Yves Tinevez, Daniel James White, Volker Hartenstein, Kevin Eliceiri, Pavel Tomancak, Albert Cardona, Fiji: an open-source platform for biological-image analysis, Nature Methods (ISSN: 1548-7105) 9 (7) (2012) 676–682, http://dx.doi.org/10.1038/nmeth.2019.

[2] Joachim Goedhart, Material Related to the Blog that Reports on the Parrot LUT, Zenodo, 2018, http://dx.doi.org/10.5281/zenodo.1211690.

[3] Hael Mughrabi, Cyclic slip irreversibilities and the evolution of fatigue damage, Metall. Mater. Trans. A (ISSN: 1543-1940) 40 (6) (2009) 1257–1279, http://dx.doi.org/10.1007/s11661-009-9839-8.

[4] Andre Pineau, Stephen D. Antolovich, High temperature fatigue of nickel-base superalloys – a review with special emphasis on deformation modes and oxidation, Eng. Fail. Anal. (ISSN: 13506307) 16 (8) (2009) 2668–2697, http://dx.doi.org/10.1016/j.engfailanal.2009.01.010, URL http://linkinghub.elsevier.com/retrieve/pii/S1350630709000259.

[5] H.S. Ho, M. Risbet, X. Feaugas, On the unified view of the contribution of plastic strain to cyclic crack initiation: Impact of the progressive transformation of shear bands to persistent slip bands, Acta Mater. (ISSN: 1359-6454) 85 (2015) 155–167, http://dx.doi.org/10.1016/j.actamat.2014.11.020, URL http://www.sciencedirect.com/science/article/pii/S1359645414008647.

[6] J. Polák, 4.01 - Cyclic deformation, crack initiation, and low-cycle fatigue, in: I. Milne, R.O. Ritchie, B. Karihaloo (Eds.), Comprehensive Structural Integrity, Pergamon, Oxford, ISBN: 978-0-08-043749-1, 2003, pp. 1–39, http://dx.doi.org/10.1016/B0-08-043749-4/04060-X, URL http://www.sciencedirect.com/science/article/pii/B008043749404060X.

[7] Campbell Laird, CHAPTER 27 - FATIGUE, in: Robert W. Cahn, Peter Haasen (Eds.), Physical Metallurgy (Fourth Edition), fourth ed., North-Holland, Oxford, ISBN: 978-0-444-89875-3, 1996, pp. 2293–2397, http://dx.doi.org/10.1016/B978-044489875-3/50032-6, URL http://www.sciencedirect.com/science/article/pii/B9780444898753500326.

[8] P. Neumann, Coarse slip model of fatigue, Acta Metall. (ISSN: 0001-6160) 17 (9) (1969) 1219–1225, http://dx.doi.org/10.1016/0001-6160(69)90099-6, URL http://www.sciencedirect.com/science/article/pii/0001616069900996.

[9] J.C. Stinville, P.G. Callahan, M.A. Charpagne, M.P. Echlin, V. Valle, T.M. Pollock, Direct measurements of slip irreversibility in a nickel-based superalloy using high resolution digital image correlation, Acta Mater. (ISSN: 1359-6454) 186 (2020) 172–189, http://dx.doi.org/10.1016/j.actamat.2019.12.009, URL http://www.sciencedirect.com/science/article/pii/S1359645419308389.

[10] H.S. Ho, M. Risbet, X. Feaugas, A cyclic slip irreversibility based model for fatigue crack initiation of nickel base alloys, Int. J. Fatigue (ISSN: 0142-1123) 102 (2017) 1–8, http://dx.doi.org/10.1016/j.ijfatigue.2017.04.007, URL http://www.sciencedirect.com/science/article/pii/S0142112317301780.

[11] Hael Mughrabi, Cyclic slip irreversibility and fatigue life: A microstructure-based analysis, Acta Mater. (ISSN: 1359-6454) 61 (4) (2013) 1197–1203, http://dx.doi.org/10.1016/j.actamat.2012.10.029, URL http://www.sciencedirect.com/science/article/pii/S1359645412007665.

[12] J.C. Stinville, M.A. Charpagne, A. Cervellon, S. Hemery, F. Wang, P.G. Callahan, V. Valle, T.M. Pollock, On the origins of fatigue strength in crystalline metallic materials, Science 377 (6610) (2022) 1065–1071, http://dx.doi.org/10.1126/science.abn0392, URL https://www.science.org/doi/abs/10.1126/science.abn0392.

[13] Allan Harte, Michael Atkinson, Albert Smith, Carsten Drouven, Stefan Zaefferer, João Quinta da Fonseca, Michael Preuss, The effect of solid solution and gamma prime on the deformation modes in Ni-based superalloys, Acta Mater. (ISSN: 1359-6454) 194 (2020) 257–275, http://dx.doi.org/10.1016/j.actamat.2020.04.004, URL https://www.sciencedirect.com/science/article/pii/S1359645420302615.

[14] Ryan Sperry, Allan Harte, João Quinta da Fonseca, Eric R Homer, Robert H Wagoner, David T Fullwood, Slip band characteristics in the presence of grain boundaries in nickel-based superalloy, Acta Mater. (ISSN: 1359-6454) 193 (2020) 229–238, http://dx.doi.org/10.1016/j.actamat.2020.04.037, URL https://www.sciencedirect.com/science/article/pii/S1359645420303025.

[15] Jiashi Miao, Tresa M. Pollock, J. Wayne Jones, Microstructural extremes and the transition from fatigue crack initiation to small crack growth in a polycrystalline nickel-base superalloy, Acta Mater. (ISSN: 1359-6454) 60 (6–7) (2012) 2840–2854, http://dx.doi.org/10.1016/j.actamat.2012.01.049, URL http://www.sciencedirect.com/science/article/pii/S1359645412000870.

[16] Donghyuk Kim, Rong Jiang, Ian Sinclair, Philippa Reed, Microstructural influences on fatigue crack initiation and early propagation in Ni-based superalloy, Mater. Sci. Technol. 38 (14) (2022) 1081–1094, http://dx.doi.org/10.1080/02670836.2022.2070336.

[17] A. Heinz, P. Neumann, Crack initiation during high cycle fatigue of an austenitic steel, Acta Metall. Mater. (ISSN: 0956-7151) 38 (10) (1990) 1933–1940, http://dx.doi.org/10.1016/0956-7151(90)90305-Z, URL http://www.sciencedirect.com/science/article/pii/095671519090305Z.

[18] Xiaoxian Zhang, Jean-Charles Stinville, Tresa M. Pollock, Fionn P.E. Dunne, Crystallography and elastic anisotropy in fatigue crack nucleation at nickel alloy twin boundaries, J. Mech. Phys. Solids (ISSN: 0022-5096) 155 (2021) 104538, http://dx.doi.org/10.1016/j.jmps.2021.104538, URL https://www.sciencedirect.com/science/article/pii/S0022509621001988.

[19] J.C. Stinville, N. Vanderesse, F. Bridier, P. Bocher, T.M. Pollock, High resolution mapping of strain localization near twin boundaries in a nickel-based superalloy, Acta Mater. (ISSN: 1359-6454) 98 (2015) 29–42, http://dx.doi.org/10.1016/j.actamat.2015.07.016, URL http://www.sciencedirect.com/science/article/pii/S1359645415004784.

[20] P. Peralta, L. Llanes, J. Bassani, C. Laird, Deformation from twin-boundary stresses and the role of texture: Application to fatigue, Phil. Mag. A 70 (1) (1994) 219–232, http://dx.doi.org/10.1080/01418619408242547.

[21] W.H. Kim, C. Laird, Crack nucleation and stage I propagation in high strain fatigue—I. microscopic and interferometric observations, Acta Metall. (ISSN: 0001-6160) 26 (5) (1978) 777–787, http://dx.doi.org/10.1016/0001-6160(78)90028-7, URL https://www.sciencedirect.com/science/article/pii/0001616078900287.

[22] M.A. Charpagne, J.M. Hestroffer, A.T. Polonsky, M.P. Echlin, D. Texier, V. Valle, I.J. Beyerlein, T.M. Pollock, J.C. Stinville, Slip localization in inconel 718: A three-dimensional and statistical perspective, Acta Mater. (ISSN: 1359-6454) 215 (2021) 117037, http://dx.doi.org/10.1016/j.actamat.2021.117037, URL https://www.sciencedirect.com/science/article/pii/S1359645421004171.

[23] Jonathan M. Hestroffer, Jean-Charles Stinville, Marie-Agathe Charpagne, Matthew P. Miller, Tresa M. Pollock, Irene J. Beyerlein, Slip localization behavior at triple junctions in nickel-base superalloys, Acta Mater. (ISSN: 1359-6454) 249 (2023) 118801, http://dx.doi.org/10.1016/j.actamat.2023.118801, URL https://www.sciencedirect.com/science/article/pii/S1359645423001325.

[24] Zhenbo Zhang, Zhibiao Yang, Song Lu, Allan Harte, Roberto Morana, Michael Preuss, Strain localisation and failure at twin-boundary complexions in nickel-based superalloys, Nature Commun. (ISSN: 2041-1723) 11 (1) (2020) 4890, http://dx.doi.org/10.1038/s41467-020-18641-z.

[25] Hariharan Sriram, Semanti Mukhopadhyay, Kamalnath Kadirvel, Rongpei Shi, Michael J. Mills, Yunzhi Wang, Formation mechanisms of coprecipitates in inconel 718 superalloys, Acta Mater. (ISSN: 1359-6454) 249 (2023) 118825, http://dx.doi.org/10.1016/j.actamat.2023.118825, URL https://www.sciencedirect.com/science/article/pii/S1359645423001568.

[26] Julien Prouteau, Patrick Villechaise, Loic Signor, Jonathan Cormier, Early stages of fatigue crack initiation in relation with twin boundaries in polycrystalline Ni-based superalloy AD730™, Metall. Mater. Trans. A (ISSN: 1543-1940) (2022) http://dx.doi.org/10.1007/s11661-022-06916-7.

[27] Baptiste Larrouy, Patrick Villechaise, Jonathan Cormier, Olivier Berteaux, Grain boundary–slip bands interactions: Impact on the fatigue crack initiation in a polycrystalline forged Ni-based superalloy, Acta Mater. (ISSN: 1359-6454) 99 (2015) 325–336, http://dx.doi.org/10.1016/j.actamat.2015.08.009, URL http://www.sciencedirect.com/science/article/pii/S135964541500573X.

[28] Patrick Villechaise, Jonathan Cormier, Thomas Billot, José Mendez, Mechanical behaviour and damage processes of Udimet 720Li: influence of localized plasticity at grain boundaries, in: 12th International Symposium on Superalloys, 2012, pp. 15–24.

[29] J.C. Stinville, W.C. Lenthe, M.P. Echlin, P.G. Callahan, D. Texier, T.M. Pollock, Microstructural statistics for fatigue crack initiation in polycrystalline nickel-base superalloys, Int. J. Fract. (ISSN: 1573-2673) (2017) http://dx.doi.org/10.1007/s10704-017-0241-z.

[30] Michael D. Sangid, Hans J. Maier, Huseyin Sehitoglu, An energy-based microstructure model to account for fatigue scatter in polycrystals, J. Mech. Phys. Solids (ISSN: 0022-5096) 59 (3) (2011) 595–609, http://dx.doi.org/10.1016/j.jmps.2010.12.014, URL https://www.sciencedirect.com/science/article/pii/S0022509610002541.

[31] Clayton A. Stein, Albert Cerrone, Tugce Ozturk, Sukbin Lee, Peter Kenesei, Harris Tucker, Reeju Pokharel, Jonathan Lind, Christopher Hefferan, Robert M. Suter, Anthony R. Ingraffea, Anthony D. Rollett, Fatigue crack initiation, slip localization and twin boundaries in a nickel-based superalloy, Curr. Opin. Solid State Mater. Sci. (ISSN: 1359-0286) 18 (4) (2014) 244–252, http://dx.doi.org/10.1016/j.cossms.2014.06.001, URL https://www.sciencedirect.com/science/article/pii/S1359028614000370. Slip Localization and Transfer in Deformation and Fatigue of Polycrystals.

[32] Damien Texier, Jonathan Cormier, Patrick Villechaise, Jean-Charles Stinville, Chris J. Torbet, Stéphane Pierret, Tresa M. Pollock, Crack initiation sensitivity of wrought direct aged alloy 718 in the very high cycle fatigue regime: the role of non-metallic inclusions, Mater. Sci. Eng. A (ISSN: 0921-5093) 678 (2016) 122–136, http://dx.doi.org/10.1016/j.msea.2016.09.098, URL https://www.sciencedirect.com/science/article/pii/S0921509316311789.

[33] J. Gayda, R.V. Miner, Fatigue crack initiation and propagation in several nickel-base superalloys at 650°C, Int. J. Fatigue (ISSN: 0142-1123) 5 (3) (1983) 135–143, http://dx.doi.org/10.1016/0142-1123(83)90026-9, URL https://www.sciencedirect.com/science/article/pii/0142112383900269.

[34] F. Di Gioacchino, T.E.J. Edwards, G.N. Wells, W.J. Clegg, A new mechanism of strain transfer in polycrystals, Sci. Rep. (ISSN: 2045-2322) 10 (1) (2020) 10082, http://dx.doi.org/10.1038/s41598-020-66569-7.

[35] J.C. Stinville, M.P. Echlin, D. Texier, F. Bridier, P. Bocher, T.M. Pollock, Sub-grain scale digital image correlation by electron microscopy for polycrystalline materials during elastic and plastic deformation, Exp. Mech. (ISSN: 0014-4851) (2015) 1–20, http://dx.doi.org/10.1007/s11340-015-0083-4.

[36] P.J.E. Forsyth, Exudation of material from slip bands at the surface of fatigued crystals of an aluminium–copper alloy, Nature (ISSN: 1476-4687) 171 (4343) (1953) 172–173, http://dx.doi.org/10.1038/171172a0.

[37] C.B. Montgomery, B. Koohbor, N.R. Sottos, A robust patterning technique for electron microscopy-based digital image correlation at sub-micron resolutions, Exp. Mech. (ISSN: 1741-2765) 59 (7) (2019) 1063–1073, http://dx.doi.org/10.1007/s11340-019-00487-2.

[38] A. Harte, M. Atkinson, M. Preuss, J. Quinta da Fonseca, A statistical study of the relationship between plastic strain and lattice misorientation on the surface of a deformed Ni-based superalloy, Acta Mater. (ISSN: 1359-6454) 195 (2020) 555–570, http://dx.doi.org/10.1016/j.actamat.2020.05.029, URL https://www.sciencedirect.com/science/article/pii/S1359645420303761.

[39] George Ellwood Dieter, David Bacon, Mechanical Metallurgy, Vol. 3, McGraw-hill New York, 1976.

[40] J.C. Stinville, M.A. Charpagne, F. Bourdin, P.G. Callahan, Z. Chen, M.P. Echlin, D. Texier, J. Cormier, P. Villechaise, T.M. Pollock, V. Valle, Measurement of elastic and rotation fields during irreversible deformation using heaviside-digital image correlation, Mater. Charact. (ISSN: 1044-5803) 169 (2020) 110600, http://dx.doi.org/10.1016/j.matchar.2020.110600, URL http://www.sciencedirect.com/science/article/pii/S1044580320320714.

[41] M.A. Charpagne, J.C. Stinville, P.G. Callahan, D. Texier, Z. Chen, P. Villechaise, V. Valle, T.M. Pollock, Automated and quantitative analysis of plastic strain localization via multi-modal data recombination, Mater. Charact. (ISSN: 1044-5803) 163 (2020) 110245, http://dx.doi.org/10.1016/j.matchar.2020.110245, URL https://www.sciencedirect.com/science/article/pii/S1044580319335569.

[42] David Fullwood, Mark Vaudin, Craig Daniels, Timothy Ruggles, Stuart I. Wright, Validation of kinematically simulated pattern HR-EBSD for measuring absolute strains and lattice tetragonality, Mater. Charact. (ISSN: 1044-5803) 107 (2015) 270–277, http://dx.doi.org/10.1016/j.matchar.2015.07.017, URL https://www.sciencedirect.com/science/article/pii/S1044580315002648.

[43] BYUOpenXY, Openxy, 2016, URL https://github.com/BYU-MicrostructureOfMaterials/OpenXY.

[44] T.J. Ruggles, D.T. Fullwood, J.W. Kysar, Resolving geometrically necessary dislocation density onto individual dislocation types using EBSD-based continuum dislocation microscopy, Int. J. Plast. (ISSN: 0749-6419) 76 (2016) 231–243, http://dx.doi.org/10.1016/j.ijplas.2015.08.005, URL https://www.sciencedirect.com/science/article/pii/S0749641915001424.

[45] Angus J. Wilkinson, Graham Meaden, David J. Dingley, Mapping strains at the nanoscale using electron back scatter diffraction, Superlattices Microstruct. (ISSN: 0749-6036) 45 (4) (2009) 285–294, http://dx.doi.org/10.1016/j.spmi.2008.10.046, URL https://www.sciencedirect.com/science/article/pii/S0749603608002462. Proceedings of the 9th International Workshop on Beam Injection Assessment of Microstructures in Semiconductors (BIAMS 2008).

[46] Angus J. Wilkinson, Graham Meaden, David J. Dingley, High-resolution elastic strain measurement from electron backscatter diffraction patterns: New levels of sensitivity, Ultramicroscopy 106 (4–5) (2006) 307–313, http://dx.doi.org/10.1016/j.ultramic.2005.10.001.

[47] G. Miyamoto, A. Shibata, T. Maki, T. Furuhara, Precise measurement of strain accommodation in austenite matrix surrounding martensite in ferrous alloys by electron backscatter diffraction analysis, Acta Mater. (ISSN: 1359-6454) 57 (4) (2009) 1120–1131, http://dx.doi.org/10.1016/j.actamat.2008.10.050, URL http://www.sciencedirect.com/science/article/pii/S1359645408008021.

[48] Y. Guo, D.M. Collins, E. Tarleton, F. Hofmann, J. Tischler, W. Liu, R. Xu, A.J. Wilkinson, T.B. Britton, Measurements of stress fields near a grain boundary: Exploring blocked arrays of dislocations in 3D, Acta Mater. (ISSN: 1359-6454) 96 (2015) 229–236, http://dx.doi.org/10.1016/j.actamat.2015.05.041, URL https://www.sciencedirect.com/science/article/pii/S1359645415003626.

[49] T.B. Britton, A.J. Wilkinson, High resolution electron backscatter diffraction measurements of elastic strain variations in the presence of larger lattice rotations, Ultramicroscopy (ISSN: 0304-3991) 114 (2012) 82–95, http://dx.doi.org/10.1016/j.ultramic.2012.01.004, URL https://www.sciencedirect.com/science/article/pii/S0304399112000058.

[50] Kathryn A. Small, Zach Clayburn, Ryan DeMott, Sophie Primig, David Fullwood, Mitra L. Taheri, Interplay of dislocation substructure and elastic strain evolution in additively manufactured inconel 625, Mater. Sci. Eng. A (ISSN: 0921-5093) 785 (2020) 139380, http://dx.doi.org/10.1016/j.msea.2020.139380, URL https://www.sciencedirect.com/science/article/pii/S0921509320304615.

[51] J.C. Stinville, J.M. Hestroffer, M.A. Charpagne, A.T. Polonsky, M.P. Echlin, C.J. Torbet, V. Valle, K.E. Nygren, M.P. Miller, O. Klaas, A. Loghin, I.J. Beyerlein, T.M. Pollock, Multi-modal dataset of a polycrystalline metallic material: 3D microstructure and deformation fields, Sci. Data (ISSN: 2052-4463) 9 (1) (2022) 460, http://dx.doi.org/10.1038/s41597-022-01525-w.

[52] McLean P. Echlin, Marcus Straw, Steven Randolph, Jorge Filevich, Tresa M. Pollock, The TriBeam system: Femtosecond laser ablation in situ SEM, Mater. Charact. 100 (2015) 1–12, http://dx.doi.org/10.1016/j.matchar.2014.10.023.

[53] Marie-Agathe Charpagne, Florian Strub, Tresa M. Pollock, Accurate reconstruction of EBSD datasets by a multimodal data approach using an evolutionary algorithm, Mater. Charact. (ISSN: 1044-5803) 150 (2019) 184–198, http://dx.doi.org/10.1016/j.matchar.2019.01.033.

[54] M.A. Charpagne, J.C. Stinville, P.G. Callahan, D. Texier, Z. Chen, P. Villechaise, V. Valle, T.M. Pollock, Automated and quantitative analysis of plastic strain localization via multi-modal data recombination, Mater. Charact. 163 (2020) 110245, http://dx.doi.org/10.1016/j.matchar.2020.110245.

[55] Michael A. Groeber, Michael A. Jackson, Dream.3D: A digital representation environment for the analysis of microstructure in 3D, Integr. Mater. Manuf. Innov. (ISSN: 2193-9772) 3 (1) (2014) 56–72, http://dx.doi.org/10.1186/2193-9772-3-5.

[56] S.R. Kalidindi, C.A. Bronkhorst, L. Anand, Crystallographic texture evolution in bulk deformation processing of FCC metals, J. Mech. Phys. Solids (ISSN: 0022-5096) 40 (3) (1992) 537–569, http://dx.doi.org/10.1016/0022-5096(92)80003-9, URL https://www.sciencedirect.com/science/article/pii/0022509692800039.

[57] G. Martin, N. Ochoa, K. Saï, E. Hervé-Luanco, G. Cailletaud, A multiscale model for the elastoviscoplastic behavior of directionally solidified alloys: Application to FE structural computations, Int. J. Solids Struct. (ISSN: 0020-7683) 51 (5) (2014) 1175–1187, http://dx.doi.org/10.1016/j.ijsolstr.2013.12.013, URL https://www.sciencedirect.com/science/article/pii/S0020768313004861.

[58] J.C. Stinville, W.C. Lenthe, J. Miao, T.M. Pollock, A combined grain scale elastic–plastic criterion for identification of fatigue crack initiation sites in a twin containing polycrystalline nickel-base superalloy, Acta Mater. (ISSN: 1359-6454) 103 (2016) 461–473, http://dx.doi.org/10.1016/j.actamat.2015.09.050, URL http://www.sciencedirect.com/science/article/pii/S1359645415007399.

[59] Valéry Valle, Stephen Hedan, Philippe Cosenza, Anne-Laure Fauchille, M. Berdjane, DIC development for the study of materials including multiple crossing cracks, Exp. Mech. (ISSN: 17412765) 55 (2) (2015) 379–391, http://dx.doi.org/10.1007/s11340-014-9948-1.

[60] J. Polák, V. Mazánová, M. Heczko, R. Petráš, I. Kuběna, L. Casalena, J. Man, The role of extrusions and intrusions in fatigue crack initiation, Eng. Fract. Mech. (ISSN: 0013-7944) 185 (2017) 46–60, http://dx.doi.org/10.1016/j.engfracmech.2017.03.006, URL https://www.sciencedirect.com/science/article/pii/S0013794416307305. XVIII International Colloquium Mechanical Fatigue of Metals.

[61] F. Bourdin, J.C. Stinville, M.P. Echlin, P.G. Callahan, W.C. Lenthe, C.J. Torbet, D. Texier, F. Bridier, J. Cormier, P. Villechaise, T.M. Pollock, V. Valle, Measurements of plastic localization by heaviside-digital image correlation, Acta Mater. (ISSN: 1359-6454) 157 (2018) 307–325, http://dx.doi.org/10.1016/j.actamat.2018.07.013, URL http://www.sciencedirect.com/science/article/pii/S135964541830541X.

[62] J. Luster, M.A. Morris, Compatibility of deformation in two-phase Ti-Al alloys: Dependence on microstructure and orientation relationships, Metall. Mater. Trans. A (ISSN: 1543-1940) 26 (7) (1995) 1745–1756, http://dx.doi.org/10.1007/BF02670762.

[63] Andre Pineau, Stephen D. Antolovich, High temperature fatigue of nickel-base superalloys – a review with special emphasis on deformation modes and oxidation, Eng. Fail. Anal. (ISSN: 1350-6307) 16 (8) (2009) 2668–2697, http://dx.doi.org/10.1016/j.engfailanal.2009.01.010, URL https://www.sciencedirect.com/science/article/pii/S1350630709000259. Special issue honouring Professor Manuel Elices on the occasion of his 70th birthday.

[64] T.H. Lin, Y.M. Ito, Fatigue crack nucleation in metals, Proc. Natl. Acad. Sci. 62 (3) (1969) 631–635, http://dx.doi.org/10.1073/pnas.62.3.631.

[65] Michael D. Sangid, The physics of fatigue crack initiation, Int. J. Fatigue (ISSN: 0142-1123) 57 (2013) 58–72, http://dx.doi.org/10.1016/j.ijfatigue.2012.10.009, URL https://www.sciencedirect.com/science/article/pii/S0142112312002940. Fatigue and Microstructure: A special issue on recent advances.

[66] Jean Charles Stinville, Etienne Martin, Mallikarjun Karadge, Shak Ismonov, Monica Soare, Tim Hanlon, Sairam Sundaram, McLean P. Echlin, Patrick G. Callahan, William C. Lenthe, V.M. Miller, Jiashi Miao, Andrew E. Wessman, Rebecca Finlay, Adrian Loghin, Judson Marte, Tresa M. Pollock, Fatigue deformation in a polycrystalline nickel base superalloy at intermediate and high temperature: Competing failure modes, Acta Mater. (ISSN: 1359-6454) 152 (2018) 16–33, http://dx.doi.org/10.1016/j.actamat.2018.03.035, URL http://www.sciencedirect.com/science/article/pii/S1359645418302337.

[67] J. Miao, T.M. Pollock, J.W. Jones, Fatigue crack initiation in nickel-based superalloy René 88 DT at 593 °C, in: Superalloys, TMS, Warrendale, PA, 2008, pp. 589–597.

[68] Kwai S. Chan, Roles of microstructure in fatigue crack initiation, Int. J. Fatigue (ISSN: 0142-1123) 32 (9) (2010) 1428–1447, http://dx.doi.org/10.1016/j.ijfatigue.2009.10.005, URL https://www.sciencedirect.com/science/article/pii/S0142112309002989. Emerging Frontiers in Fatigue.

[69] Ali Riza Durmaz, Erik Natkowski, Nikolai Arnaudov, Petra Sonnweber-Ribic, Stefan Weihe, Sebastian Münstermann, Chris Eberl, Peter Gumbsch, Micromechanical fatigue experiments for validation of microstructure-sensitive fatigue simulation models, Int. J. Fatigue (ISSN: 0142-1123) 160 (2022) 106824, http://dx.doi.org/10.1016/j.ijfatigue.2022.106824, URL https://www.sciencedirect.com/science/article/pii/S0142112322000998.

[70] Mohsen Taheri Andani, Aaditya Lakshmanan, Mohammadreza Karamooz-Ravari, Veera Sundararaghavan, John Allison, Amit Misra, A quantitative study of stress fields ahead of a slip band blocked by a grain boundary in unalloyed magnesium, Sci. Rep. (ISSN: 2045-2322) 10 (1) (2020) 3084, http://dx.doi.org/10.1038/s41598-020-59684-y.

[71] Y. Guo, T.B. Britton, A.J. Wilkinson, Slip band–grain boundary interactions in commercial-purity titanium, Acta Mater. (ISSN: 1359-6454) 76 (2014) 1–12, http://dx.doi.org/10.1016/j.actamat.2014.05.015, URL http://www.sciencedirect.com/science/article/pii/S1359645414003632.

[72] S. Haouala, R. Alizadeh, T.R. Bieler, J. Segurado, J. LLorca, Effect of slip transmission at grain boundaries in al bicrystals, Int. J. Plast. (ISSN: 0749-6419) 126 (2020) 102600, http://dx.doi.org/10.1016/j.ijplas.2019.09.006, URL https://www.sciencedirect.com/science/article/pii/S0749641919303456.

[73] Dayong An, Xinxi Liu, Yanqi Liu, Xifeng Li, Jun Chen, Experimental investigation of dislocation-grain boundary interaction in coarse-grained high–manganese steels using quasi in situ electron channelling contrast imaging, Mater. Charact. (ISSN: 1044-5803) 195 (2023) 112545, http://dx.doi.org/10.1016/j.matchar.2022.112545, URL https://www.sciencedirect.com/science/article/pii/S1044580322008270.

[74] Yipeng Peng, Rigelesaiyin Ji, Thanh Phan, Wei Gao, Valery I. Levitas, Liming Xiong, An atomistic-to-microscale computational analysis of the dislocation pileup-induced local stresses near an interface in plastically deformed two-phase materials, Acta Mater. (ISSN: 1359-6454) 226 (2022) 117663, http://dx.doi.org/10.1016/j.actamat.2022.117663, URL https://www.sciencedirect.com/science/article/pii/S1359645422000489.

[75] T.R. Bieler, P. Eisenlohr, F. Roters, D. Kumar, D.E. Mason, M.A. Crimp, D. Raabe, The role of heterogeneous deformation on damage nucleation at grain boundaries in single phase metals, Int. J. Plast. (ISSN: 0749-6419) 25 (9) (2009) 1655–1683, http://dx.doi.org/10.1016/j.ijplas.2008.09.002, URL https://www.sciencedirect.com/science/article/pii/S074964190800140X. Exploring New Horizons of Metal Forming Research.

[76] Wael Z. Abuzaid, Michael D. Sangid, Jay D. Carroll, Huseyin Sehitoglu, John Lambros, Slip transfer and plastic strain accumulation across grain boundaries in Hastelloy X, J. Mech. Phys. Solids (ISSN: 0022-5096) 60 (6) (2012) 1201–1220, http://dx.doi.org/10.1016/j.jmps.2012.02.001, URL http://www.sciencedirect.com/science/article/pii/S0022509612000324.

[77] Andrea Rovinelli, Ricardo A. Lebensohn, Michael D. Sangid, Influence of microstructure variability on short crack behavior through postulated micromechanical short crack driving force metrics, Eng. Fract. Mech. 138 (2015) 265–288.

[78] Michael D. Sangid, Hans J. Maier, Huseyin Sehitoglu, The role of grain boundaries on fatigue crack initiation–an energy approach, Int. J. Plast. 27 (5) (2011) 801–821.

[79] V.V.C. Wan, D.W. MacLachlan, FPE Dunne, Integrated experiment and modelling of microstructurally-sensitive crack growth, Int. J. Fatigue 91 (2016) 110–123.

[80] Bo Chen, Jun Jiang, Fionn P.E. Dunne, Is stored energy density the primary meso-scale mechanistic driver for fatigue crack nucleation? Int. J. Plast. 101 (2018) 213–229.

[81] Gustavo M Castelluccio, William D Musinski, David L McDowell, Recent developments in assessing microstructure-sensitive early stage fatigue of polycrystals, Curr. Opin. Solid State Mater. Sci. 18 (4) (2014) 180–187.

[82] Wenbin Liu, Ying Liu, Haonan Sui, Lirong Chen, Long Yu, Xin Yi, Huiling Duan, Dislocation-grain boundary interaction in metallic materials: Competition between dislocation transmission and dislocation source activation, J. Mech. Phys. Solids (ISSN: 0022-5096) 145 (2020) 104158, http://dx.doi.org/10.1016/j.jmps.2020.104158, URL https://www.sciencedirect.com/science/article/pii/S0022509620303914.

[83] R.L. Black, T. Garbowski, C. Bean, A.L. Eberle, S. Nickell, D. Texier, V. Valle, J.C. Stinville, High-throughput high-resolution digital image correlation measurements by multi-beam SEM imaging, Exp. Mech. (ISSN: 1741-2765) 63 (5) (2023) 939–953, http://dx.doi.org/10.1007/s11340-023-00961-y.

[84] Michael D. Sangid, Tawhid Ezaz, Huseyin Sehitoglu, Ian M. Robertson, Energy of slip transmission and nucleation at grain boundaries, Acta Mater. (ISSN: 1359-6454) 59 (1) (2011) 283–296, http://dx.doi.org/10.1016/j.actamat.2010.09.032, URL https://www.sciencedirect.com/science/article/pii/S1359645410006099.

[85] Behnam Ahmadikia, M. Arul Kumar, Irene J. Beyerlein, Effect of neighboring grain orientation on strain localization in slip bands in HCP materials, Int. J. Plast. (ISSN: 0749-6419) 144 (2021) 103026, http://dx.doi.org/10.1016/j.ijplas.2021.103026, URL https://www.sciencedirect.com/science/article/pii/S0749641921001017.

[86] Peter Gudmundson, A unified treatment of strain gradient plasticity, J. Mech. Phys. Solids (ISSN: 0022-5096) 52 (6) (2004) 1379–1406, http://dx.doi.org/10.1016/j.jmps.2003.11.002, URL https://www.sciencedirect.com/science/article/pii/S0022509603001959.